An improved method for calculating flow past flapping and hovering airfoils

T.K. Sengupta[†], V. Vikas[‡] and A. Johri[†]

[†] *Department of Aerospace Engineering, I.I.T. Kanpur, U.P. 208016, India; e-mail: tksen@iitk.ac.in and*

[‡] *Department of Aerospace Engineering, I.I.T. Kharagpur, W. Bengal 741302, India*

A method is reported here for calculating unsteady aerodynamics of hovering and flapping airfoil for two- dimensional flow via the following improved methodologies: (a) a correct formulation of the problem using stream function (ψ) and vorticity (ω) as dependent variables; (b) calculating loads and moment by a new method to solve the governing pressure Poisson equation (PPE) in a truncated part of the computational domain on a non-staggered grid; (c) accurate solution using high accuracy compact difference scheme for the vorticity transport equation (VTE) and (d) accelerating the computations by using a high order filter after each time step of integration. These have been used to solve Navier-Stokes equation for flow past flapping and hovering NACA 0014 and 0015 airfoils at typical Reynolds numbers relevant to the study of unsteady aerodynamics of micro air vehicle (MAV) and insect/ bird flight.

Key Words: Stream function- vorticity formulation, Pressure Poisson equation, compact schemes, Navier-Stokes equation, unsteady aerodynamics, flapping and hovering flight

0. INTRODUCTION

Computing unsteady flows at low to moderate Reynolds numbers continues to be of significant interest due to its application in MAVs and its relevance to insect and bird flights. Flapping and hovering flight of bird and insect are fine examples of optimum motion of aerodynamic surfaces that simultaneously develop necessary thrust for forward motion and sustained lift to keep it airborne. This is totally different from aircraft motion where lift and thrust are created by different subsystems. Also, lift and thrust are created in aircraft by steady flow devices, while natural fliers use unsteady aerodynamics to create the same by articulating same surfaces. Comprehensive reviews of the subject can be found in [**?**]- [**?**]. While biologists have focused attention on kinematics of motion for birds and insects (see [**?**], [**?**] for example), bio-fluid-dynamicists have attempted to explain mechanisms of flights based on simplified models in the limit of quasi-steady and unsteady operation. Recent interest in engineering community on bird and insect flight is the requirement of flying payload carrying flight vehicles that are very small in dimension and weight for their perceived mission requirements. With restriction on size of such devices (around 15 cm or less) and speed regimes (of about 10 m/sec)- the operating Reynolds numbers are in the range of 10^4 to 10^5. Such flows display massive boundary layer separation, flow transition and large vortical structures that make theoretical and experimental studies a formidable task. At the same time, birds and insects flying with similar parameters display extraordinary maneuverability, agility and low-speed flying capability and even the ability to hover. To mimic such modes of flight in man-made devices, it is essential to understand and model such dynamics. In general, bird/ insect flight is due to complex combinations of translational and angular motion of lifting surfaces. It is understood that

the flow dynamics is viscous in nature at the relevant moderate Reynolds number. Understanding complex phase relationships between wing kinematics and system response is central to design any engineering devices delivering simultaneously high aerodynamic and propulsive efficiencies. Experimental studies are difficult and existing state of art is discussed in [?]-, [?]. Of particular interest are the visual signatures of wing kinematics recorded in e.g. Tobalske & Dial [?] and Nachtigall [?]. Freymuth [?] has experimentally investigated the motion of an airfoil in combined harmonic plunging and pitching oscillatory motion with phase difference to generate thrust in still air environment. The role of vortex street acting as a jet stream in the wake is discussed in [?] as the mechanism for generating lift and thrust. The author identified three generic cases of hover mode. Zero baseline angle of attack of the airfoil with ninety degrees phase difference between horizontal and pitch oscillation is termed as the first-hover or the water-treading mode. In the second-hover or degenerate figure of eight mode, the baseline angle of attack is ninety degrees and pitching oscillation has a phase lag of ninety degrees with respect to translational oscillation. For the third- mode, also called the oblique or dragonfly mode, the lifting surface is at an angle of attack nominally between zero and ninety degrees while the phase difference between horizontal and pitch oscillations is kept close to ninety degrees. In the present study, the second hover mode case will be computed and analyzed.

It is now accepted that theoretical studies involving steady-state aerodynamics is of limited value and some unsteady flow models have been studied. For example, in [?] a flapping wing inviscid flow model has been proposed and Spedding [?] provides an extensive review of early aerodynamic models of flapping flight. However, it is essential that any unsteady flow model must include viscous effects involving separation and transition in the presence of large vortices. This has been attempted by using CFD techniques to study flapping flight, where the airfoil executes heaving oscillations being placed in an uniform flow. In [?] a commercial software, based on finite volume primitive variable formulation is used to solve Navier- Stokes equation in Lagrangian- Eulerian framework. The authors remark that it is essential to satisfy the conservation law, otherwise false mass is created leading to large errors. In [?], three- dimensional incompressible Navier-Stokes equation in primitive variables have been solved in strong conservation form using SIMPLEC and PISO methods. Sun & Tang [?] have reported solving three- dimensional Navier- Stokes equation using the artificial compressibility method of [?]. In [?], spatial discretization was performed by third order upwind flux-difference splitting and time integration by second order Adams- Bashforth technique. Relatively good agreement was reported with experimental data. However, this time integration strategy displays spurious computational mode with large error for unsteady flows (see [?] for details).

Ideally, three-dimensional computation around a deforming wing is desirable to understand the fluid dynamics of flapping and hover modes of motion. The present day situation remains the same as was noted earlier by Wang [?] that *from a practical point of view, while it is possible to resolve two-dimensional flows at Reynolds numbers relevant to insect flight, it remains to be seen whether one can do the same for three-dimensional flows.* This is due to problems of resolving length and time scales involved in solution of unsteady Navier- Stokes equation while satisfying mass conservation accurately in primitive variable formulations. This is avoided in

computing two-dimensional flows given by Navier- Stokes equation using stream function-vorticity ($\psi - \omega$) formulation. This equation satisfies mass conservation identically and allows taking larger number of grid points as the number of unknowns reduces from three to two. Gustafson & Leben [?] and Gustafson et al. [?] have used this formulation to compute hovering flight of an elliptic cylinder. Unfortunately, the governing VTE written in the moving frame had an important angular acceleration term omitted erroneously. This term is essential for hovering flight, with the lifting surface executing pitching oscillations. In [?] same formulation is used, but the considered heaving oscillation in an uniform flow does not require this angular acceleration term. For the flapping motion vortex shedding was investigated in [?] and an optimal flapping frequency based on time scales associated with shedding of leading and trailing edge vortices is reported. In solving the problem a fourth-order compact finite difference scheme, developed in [?] is used. In [?] - [?], the Navier- Stokes equation is solved for an elliptic airfoil and results are qualitatively compared with the experiments of [?] that was performed with an airfoil with rectangular cross section with rounded off edges of significantly lower thickness ratio. Choice of elliptic airfoil allows creating orthogonal grid that is known to yield accurate numerical solution of Navier- Stokes equation. However, in [?] - [?] loads and moment are calculated by quadrature of the vorticity field - a technique known for its limitation as discussed in [?] and [?] in details. In [?] and [?], instead the solution of PPE is suggested to get accurate loads and moment calculation- a procedure followed here.

Based on above discussions, a reformulation of the problem is necessary to study general flapping and hover mode of motion in two-dimensions for an actual airfoil. To account for an actual airfoil, one can construct orthogonal grids following the method proposed in [?]. Here the PPE is solved using the orthogonal non-staggered grid by a new method to calculate loads and moment. This is done by solving the PPE in a sub-domain with exact boundary conditions on sub-domain boundaries. This is a significant improvement over the method in [?] that was developed for steady flow problems solved in Cartesian grids. Furthermore, a very high spectral accuracy compact scheme is used here along with a high order filter applied to the solution at the end of every time step. Both of these accelerate computations by orders of magnitude (more than hundred-folds) in solving NS equation for flapping and hovering airfoils at moderate Reynolds numbers. Ideas of [?] for calculating PPE have also been used in [?] and [?] for further development.

In a combined experimental and computational investigation for flapping wing aerodynamics, Jones et al. [?] reported results that included wind tunnel investigation on finite aspect ratio wing to directly measure forces, time- accurate LDV measurements and flow visualization for a NACA 0014 airfoil. Two- and three-dimensional Navier- Stokes and Euler solutions were also obtained computationally and compared with experimental results with limited success. The airfoil in the experiments were made to execute only plunging oscillation given by,

$$y(t) = hcos(kt) \tag{1}$$

A plunge amplitude of $h = 0.4c$ was considered for a range of reduced frequencies, k for different angles of attack. In the present work, this geometry and motion is

considered to compute the flow field for $Re = 20000$ when the airfoil is set at zero angle of attack and the reduced frequency is $k = 0.4$. In addition to this, the second-hover mode case of [?] is computed for oscillating NACA 0015 airfoil in the pitch plane with the rotating center at the mid-chord for $Re = 27000$. In [?] the Reynolds number was chosen less than $Re = 600$, while the case computed in [?] corresponds to $Re = 1700$ for a different geometry. According to the definition of this mode of motion, the mean angle of attack is 90^o with the pitching angle oscillation amplitude was 5^o in [?]. The airfoil executed horizontal oscillation with an amplitude that is equal to the chord of the airfoil. In addition to these two cases, a combined flapping-hover mode of motion is also computed here for which no definitive results exist- but that seems to be closer to the actual case in the natural world.

It is to be noted that the present problem has similarities with the unsteady airfoil aerodynamics often studied for rotary wing devices. Some experimental and numerical contribution in this field are recorded in [?]- [?] and other references contained therein. However, we note that the Reynolds number ranges are much higher for helicopter rotor blades and flow behavior is qualitatively different that is encountered in rotary wings and that in insect and bird flights.

The paper is structured in the following manner. In the next section governing equations are given in both the inertial and non-inertial frames for the kinematics, kinetics and the governing PPE. In section 2, the numerical methods used for the various solvers are detailed. In section 3, results for various cases considered for the individual flapping, hover and a combined flapping- hover mode motion are discussed. The paper closes with few concluding remarks in section 4.

1. GOVERNING EQUATIONS IN INERTIAL AND NON-INERTIAL FRAMES

In the following, the equations are derived for both the inertial and the moving frame of reference with variables/operators represented with a subscript I indicating the quantities in the inertial frame and a subscript r indicating the corresponding moving frame quantities. The Navier-Stokes equation written in inertial frame is given by,

$$\frac{\partial \vec{V_I}}{\partial t} + \vec{V_I} \cdot \nabla \vec{V_I} = -\frac{1}{\rho}\nabla p + \nu \nabla^2 \vec{V_I} \tag{2}$$

The same equation can be written down for the moving frame of reference, whose origin translates with a velocity $\vec{V_{OI}}$ and rotates with an angular velocity $\vec{\Omega}$ with respect to the inertial frame, by the following

$$\frac{\partial \vec{V_r}}{\partial t} + 2(\vec{\Omega} \times \vec{V_r}) + (\vec{\Omega} \times \vec{\Omega} \times \vec{R_r}) + \frac{\partial \vec{\Omega}}{\partial t} \times \vec{R_r} + \vec{V_r} \cdot \nabla \vec{V_r} = -\frac{1}{\rho}\nabla p + \nu \nabla^2 \vec{V_r} \tag{3}$$

the local acceleration terms are obtained in the respective reference frames and $\vec{R_r}$ represents the position vector of any field point with respect to the moving frame of reference. The gradient and the Laplacian operators are the same for both the reference frames. Corresponding vorticity transport equations (VTEs) for the two-

dimensional flows are obtained by taking curl of Eqs. (2) and (3) and are given respectively by,

$$\frac{\partial \vec{\omega_I}}{\partial t} + (\vec{V_I} \cdot \nabla)\vec{\omega_I} = \nu \nabla^2 \vec{\omega_I} \tag{4}$$

$$\frac{\partial \vec{\omega_r}}{\partial t} + (\vec{V_r} \cdot \nabla)\vec{\omega_r} = \nu \nabla^2 \vec{\omega_r} - 2\frac{\partial \vec{\Omega}}{\partial t} \tag{5}$$

where ω_I is the out-of-plane component of vorticity defined by $\omega_I = (\nabla \times V_I).\hat{k}$ and hence the vortex stretching terms are absent for the considered two-dimensional flow. In [**?**] and [**?**] the last term on the right hand side Eq. (5) was omitted. The velocity is related to the stream function by $V_I = \nabla \times \Psi_I$, where $\Psi_I = (0, 0, \psi_I)$. Similarly one can relate the vorticity, velocity and stream function for the moving frame of reference. The stream function is related to the corresponding vorticity fields by the kinematic definitions expressed as the stream function equations (SFEs) given by, $\nabla^2 \psi_I = -\omega_I$ and $\nabla^2 \psi_r = -\omega_r$. Also, the vorticity fields in the inertial and moving frame of references are related by $\omega_I = \omega_r + 2\Omega$. The stream function for the inertial and moving frame of references are also related as,

$$\psi_I = \psi_r - \frac{\Omega}{2} R_r^2 + f(x_r, y_r) \tag{6}$$

with f an unknown function that can be defined in terms of the velocity field. However, one can define a new stream function, ψ_N by,

$$\psi_N = \psi_r - \frac{\Omega}{2}(R_r^2 - R_{oI}^2 + u_{oI} y_I - v_{oI} x_I) \tag{7}$$

such that ψ_N satisfies the Poisson equation:$\nabla^2 \psi_N = -\omega_I$. The motion of the origin of the moving frame of reference is defined by the following relationships,

$$x_{oI} = (x_{oI})_m + a_x cos(k_x t) \tag{8}$$

$$y_{oI} = (y_{oI})_m + a_y cos(k_y t) \tag{9}$$

and the pitching motion of the airfoil is given by,

$$\alpha = \alpha_m + \alpha_a cos(k_\alpha t + \phi) \tag{10}$$

In the above, quantities with subscript m signify mean quantities and ϕ is the phase difference between the pitching and heaving/ horizontal oscillation executed by the airfoil. It is, in general, possible to prescribe different reduced frequencies for the translational and rotational motion of the airfoil.

The stream function- vorticity formulation avoids the problems of pressure- velocity coupling and satisfaction of mass conservation everywhere in the flow field as opposed to the primitive variable formulation. However, to calculate the load accurately, one needs to solve a pressure Poisson equation instead. This can be performed by taking the divergence of Eqs. (2) and (3) and after some simplification yields the following,

$$\nabla^2(\frac{p}{\rho}+\frac{V_I^2}{2}) = \nabla\cdot(\vec{V_I}\times\vec{\omega_I}) \tag{11}$$

and

$$\nabla^2(\frac{p}{\rho}+\frac{V_r^2}{2}) = \vec{V_r}\cdot\nabla^2\vec{V_r}+\omega_r^2) + 2\vec{\Omega}\cdot\vec{\omega_r} \tag{12}$$

The quantity in parenthesis, on the left hand side of above is the total pressure (p_t) and is a good measure of mechanical energy of the flow. To calculate the loads and moment, it would be preferable to solve Eq. (11), as it involves calculating fewer terms. Above equations are solved in appropriate non- dimensional forms that are obtained by introducing relevant length (c) and velocity (U_o) scales. The non-dimensional VTE that is solved is given by,

$$\frac{\partial\vec{\omega_r}}{\partial t}+(\vec{V_r}\cdot\nabla)\vec{\omega_r} = \frac{1}{Re}\nabla^2\vec{\omega_r} - 2\frac{\partial\vec{\Omega}}{\partial t} \tag{13}$$

where the Reynolds number is given by $Re=\frac{U_o c}{\nu}$ with c as the chord of the airfoil. The vorticities, frequencies and angular rotation rates are non-dimensionalized by $\frac{U_o}{c}$. For the flapping motion, the oncoming free-stream speed is chosen as the velocity scale.

The velocity field for a given vorticity distribution is calculated by solving two Poisson equations given by,

$$\nabla^2\psi_I = -\omega_I \tag{14}$$

$$\nabla^2\psi_N = -\omega_I \tag{15}$$

Having obtained the velocity and vorticity field, one solves the PPE given by Eq. (11) to obtain the pressure field. Obtained pressure and vorticity fields are integrated to calculate the pressure and viscous forces acting on the airfoil. Note that the kinematic parameters of the airfoil motion given in Eqs. (8) to (10) retains the same form when non-dimensionalized. For the pure hover mode of motion, when the airfoil oscillates in pitch and in horizontal direction in the absence of mean motion, the velocity scale is taken as $\frac{k_x}{2\pi}c$.

2. NUMERICAL METHOD

The governing equations (11), (13)-(15) are solved in a body-fitted orthogonal grid around the NACA 0014 airfoil for the flapping mode motion reported in [**?**]. Same airfoil is also used to study a combined flapping and hover mode motion. However, for the second hover mode the flow is studied for a NACA 0015 airfoil-the same thickness ratio used in [**?**] for an elliptic cylinder. For external flow problems, one can follow the method of [**?**] to generate orthogonal grids. In Fig. 1, used grid for a NACA 0014 airfoil is shown where 257 points are taken in the azimuthal direction (ξ), while 300 points are taken in the wall normal direction (η). The outer boundary is located at 22.5 times the chord of the airfoil. A fourth

order curve is fitted between 99.7% of chord and the trailing edge of the airfoil, so that we have unique normal at every point on the airfoil surface. While fitting this curve, the surface and the slope is treated as continuous at the junction and passing through the trailing edge. The grid is clustered in the wall normal direction toward the airfoil surface so that the points in this direction are distributed by the parametric formula given by,

$$S(\eta) = H\left[1 - \frac{tanh[\beta(1-2\eta)]}{tanh[\beta]}\right] \tag{16}$$

with $\beta = 1.55$ chosen for appropriate clustering. Here the physical domain is mapped in $0 \leq \eta \leq 0.5$ when $S(\eta)$ varied between 0 and H. The choice of this analytic transformation is deliberate, as the corresponding metric displays three spikes only in the spectral plane and thus would have very little or no aliasing error. The points in the azimuthal direction are obtained by a cosine distribution with points clustered near the leading and trailing edges. Grids shown in Fig. 1 also show high concentration of points in the azimuthal direction originating from the near vicinity of trailing edge as two dense bands. This type of grid shock restricts the choice of large time steps. This issue is discussed further while talking about the VTE solver. In the following, various solvers for different equations are described.

2.1. Stream function equation solver

Eqs. (14) and (15) can be written down in generalized curvilinear orthogonal coordinate system as

$$\frac{\partial}{\partial\xi}\left[\frac{h_2}{h_1}\frac{\partial\psi_I}{\partial\xi}\right] + \frac{\partial}{\partial\eta}\left[\frac{h_1}{h_2}\frac{\partial\psi_I}{\partial\eta}\right] = -h_1 h_2 \omega_I \tag{17}$$

where h_1 and h_2 are the scale factors defined by

$$h_1^2 = \left(\frac{\partial x}{\partial\xi}\right)^2 + \left(\frac{\partial y}{\partial\xi}\right)^2$$

and

$$h_2^2 = \left(\frac{\partial x}{\partial\eta}\right)^2 + \left(\frac{\partial y}{\partial\eta}\right)^2$$

Similar representation can be written down for Eq. (15). To solve these two Poisson equations, on the surface of the airfoil no-slip condition is used while at the far-field the Neumann boundary conditions have been used: $\frac{\partial\psi_I}{\partial\eta} = U_o\frac{\partial y}{\partial\eta}$ and $\frac{\partial\psi_N}{\partial\eta} = U_o\frac{\partial y}{\partial\eta}$. The Poisson equations for stream functions are solved by the Strongly Implicit Procedure (SIP) as given in [**?**]. Instead of using the nine-point representation of [**?**], a five point finite difference formula is used here employing second order central differencing.

2.2. VTE solver

The VTE written in the moving frame of reference in non-dimensional form is given by Eq. (13). This is written for the generalized curvilinear orthogonal coordinates as,

$$h_1 h_2 \frac{\partial \omega_r}{\partial t} + h_2 u \frac{\partial \omega_r}{\partial \xi} + h_1 v \frac{\partial \omega_r}{\partial \eta} = \frac{1}{Re}\left[\frac{\partial}{\partial \xi}\left(\frac{h_2}{h_1}\frac{\partial \omega_r}{\partial \xi}\right) + \frac{\partial}{\partial \eta}\left(\frac{h_1}{h_2}\frac{\partial \omega_r}{\partial \eta}\right)\right] - 2\dot{\Omega} h_1 h_2 \quad (18)$$

The diffusion terms of this equation are discretized by standard second order central differencing- as they appear in self-adjoint form. The associated linear algebraic equations are then in positive definite form that converges easily. Despite the linearity of these terms, computing the above equation at lower Reynolds number suffers from effects of aliasing error that does not create problems at higher Reynolds number due to the division by the higher value of Re. Aliasing problem can be avoided by creating smoothly varying grids that does not show *grid-shocks*. Discussion about aliasing error of diffusion terms have been provided in details for different grid types in [**?**]. In solving VTE, we distinguish between two types of problems when Dirichlet boundary conditions are prescribed- in the first type, the vorticity and its derivatives are periodic (as in the ξ direction) and for the other type where the vorticity is non-periodic. In choosing very high spectral accuracy compact schemes to evaluate first derivatives (indicated by primed quantities below), a general recursion relation of the following form is used,

$$b_{j-1} u'_{j-1} + b_j u'_j + b_{j+1} u'_{j+1} = \frac{1}{h} \sum_{k=-2}^{2} a_{j+k} u_{j+k} \quad (19)$$

In the periodic direction, the discretization error is minimized if one chooses the following coefficients in the above equation [**?**]: $b_{j\pm1} = 0.3793894912$; $b_j = 1$;$a_{j\pm1} = \pm 0.7877868$; $a_{j\pm2} = \pm 0.0458012$ and $a_j = 0$. One solves the periodic tridiagonal system to evaluate the required first derivatives in this direction. While this scheme is formally second order accurate, the spectral accuracy obtained by this is one of highest among all known compact schemes.

In the non-periodic direction, one needs stable boundary closure schemes and the ones used here for the first and second node are [**?**], [**?**],

$$u'_1 = \frac{(-3u_1 + 4u_2 - u_3)}{2h} \quad (20)$$

$$u'_2 = [(\frac{2\beta}{3} - \frac{1}{3})u_1 - (\frac{8\beta}{3} + \frac{1}{2})u_2 + (4\beta + 1)u_3 - (\frac{8\beta}{3} + \frac{1}{6})u_4 + \frac{2\beta}{3}u_5]/h \quad (21)$$

with β as a parameter chosen to ensure accuracy and stability. Similar set of closure relations are employed for the other end (at $j = N$ and $N-1$) of the non-periodic direction. For the optimum performance, we have used $\beta = -0.025$ for $j = 2$ and $\beta = 0.09$ for $j = N-1$. Here, one solves a tridiagonal system to obtain the derivatives with respect to η for the vorticity employing this method. To numerically stabilize computations, an explicit fourth-order dissipation term is added to the calculated first derivatives.

Four stage Runge- Kutta scheme is used to time advance the above equation. For the grids shown in Fig. 1, when the flapping motion case was computed, it was noticed that only a very small time step is allowed for the solution of Navier- Stokes equation. This stiff time-step restriction can be significantly relaxed by filtering

the vorticity values in the azimuthal direction after each step of time integration of VTE. As this direction is periodic, the eighth order filter of [**?**] (given by Eq. (15) of the reference with the coefficients provided in Table IV) with $\alpha_f = 0.49$ is used for filtering the time- integrated vorticity values. The filtering allows to increase the time-step by two orders of magnitude to $1.0E-05$.

To solve the VTE, the required condition at the outer boundary is obtained by taking the vorticity equal to -2Ω. On the airfoil surface vorticity is continually created due to the requirement of no-slip condition. From Eq. (17), one can calculate the wall vorticity as

$$\omega_r|_{body} = -\frac{1}{h_2^2}\frac{\partial^2 \psi_r}{\partial \eta^2}|_{body} \tag{22}$$

After obtaining the velocity field by solving Eq. (17), new wall vorticity is calculated from Eq. (22) that is used as the boundary condition for integrating the VTE given by Eq. (18). At the cut- originating from the trailing edge of the airfoil- periodic boundary condition is applied for the vorticity.

2.3. Pressure solver

For the orthogonal curvilinear co-ordinate system the governing PPE given by Eq. (11) can be rewritten as,

$$\frac{\partial}{\partial \xi}(\frac{h_2}{h_1}\frac{\partial P_I}{\partial \xi}) + \frac{\partial}{\partial \eta}(\frac{h_1}{h_2}\frac{\partial P_I}{\partial \eta}) = \frac{\partial}{\partial \xi}(h_2 v_I \omega_I) - \frac{\partial}{\partial \eta}(h_1 u_I \omega_I) \tag{23}$$

where $P_I = \frac{p}{\rho} + \frac{V_I^2}{2}$, $u_I = \frac{1}{h_2}\frac{\partial \psi_I}{\partial \eta}$ and $v_I = -\frac{1}{h_1}\frac{\partial \psi_I}{\partial \xi}$.

Equation (23) is solved subject to the boundary condition derived from the normal momentum equation as applied on the airfoil and the outer boundary. These are obtained from the normal (η) momentum equation given by,

$$\frac{h_1}{h_2}\frac{\partial P_I}{\partial \eta} = -h_1 u_I \omega_I + \frac{1}{Re}\frac{\partial \omega_I}{\partial \xi} - h_1 \frac{\partial v_I}{\partial t} \tag{24}$$

Unlike other boundary conditions used in CFD over truncated domain, this boundary condition is exact. For this reason, it is possible to truncate the domain to obtain the pressure field and also to calculate loads separately for multiply connected domains. In doing so the accuracy of the load calculated is not compromised if a consistent differencing of the equation and boundary conditions are used. This is discussed next, where we extend the procedure of [**?**] to the more general case solved here. In Abdallah [**?**] only the steady state boundary condition was considered in a Cartesian frame with uniform non-staggered grid system for a driven cavity problem. Presented formulation for the PPE is one major development reported here. The case considered here, does not require that the Neumann boundary condition to be steady at the far-field boundary. Also the problem solved here is in a curvilinear orthogonal clustered grid system.

Abdallah [**?**] has shown that the existence of solution for PPE requires the satisfaction of a compatibility condition that relates the source terms with the Neumann boundary condition- a consequence of applying the Green's theorem for the PPE. This condition is not satisfied automatically in a non-staggered grid system and

solution drifts without convergence. This is explained for the Poisson equation: $\nabla^2 P = \sigma$ in a two-dimensional plane. Existence of the solution to this with Neumann boundary condition requires upon application of divergence theorem,

$$\iint\limits_{Area} \sigma dA = \oint \frac{\partial P}{\partial \eta} dl \tag{25}$$

It has been shown in [**?**] that satisfying (25) is equivalent to the following identities:

$$LHM = RHM = 0 \tag{26}$$

Where the LHM and RHM are the finite difference analog of the left and right hand side respectively for Eqs. (23) and (24) summed over all the nodes in the computing domain. To ensure that this is indeed true, specific stencils are to be chosen for the discretization. For example, Eq. (23) is discretized as,

$$\begin{aligned}
&\frac{1}{\Delta\xi^2}\left(\frac{h_2}{h_1}|_{(i+1/2,j)} P_{I(i+1,j)} + \frac{h_2}{h_1}|_{(i-1/2,j)} P_{I(i-1,j)}\right) - \\
&\left(\frac{1}{\Delta\xi^2}[\frac{h_2}{h_1}|_{(i+1/2,j)} + \frac{h_2}{h_1}|_{(i-1/2,j)}] + \frac{1}{\Delta\eta^2}[\frac{h_1}{h_2}|_{(i,j+1/2)} + \frac{h_1}{h_2}|_{(i,j-1/2)}]\right) P_{I(i,j)} + \\
&\frac{1}{\Delta\eta^2}\left(\frac{h_1}{h_2}|_{(i,j+1/2)} P_{I(i,j+1)} + \frac{h_1}{h_2}|_{(i,j-1/2)} P_{I(i,j-1)}\right) \\
&= \frac{(h_2 v\omega)_{(i+1/2,j)} - (h_2 v\omega)_{(i-1/2,j)}}{\Delta\xi} - \frac{(h_1 u\omega)_{(i,j+1/2)} - (h_1 u\omega)_{(i,j-1/2)}}{\Delta\eta}
\end{aligned} \tag{27}$$

for $(2 \le i \le n)$ and $(2 \le j \le m)$, where the subscript i denotes constant $\xi-$ lines and the subscript j denotes constant η -lines. The half-node quantities are taken as the arithmetic average of adjacent cell values. The right hand side quantities of Eq. (27) are discretized in the following manner,

$$\begin{aligned}
(h_2 v\omega)_{(i+1/2,j)} &= \frac{1}{8}\{h_2|_{(i,j)} + h_2|_{(i+1,j)}\}\{v_{(i,j)} + v_{(i+1,j)}\}\{\omega_{(i,j)} + \omega_{(i+1,j)}\} \\
(h_2 v\omega)_{(i-1/2,j)} &= \frac{1}{8}\{h_2|_{(i,j)} + h_2|_{(i-1,j)}\}\{v_{(i,j)} + v_{(i-1,j)}\}\{\omega_{(i,j)} + \omega_{(i-1,j)}\} \\
(h_1 u\omega)_{(i,j+1/2)} &= \frac{1}{8}\{h_1|_{(i,j)} + h_1|_{(i,j+1)}\}\{\omega_{(i,j)} + \omega_{(i,j+1)}\}\{u_{(i,j)} + u_{(i,j+1)}\} \\
(h_1 u\omega)_{(i,j-1/2)} &= \frac{1}{8}\{h_1|_{(i,j)} + h_1|_{(i,j-1)}\}\{\omega_{(i,j)} + \omega_{(i,j-1)}\}\{u_{(i,j)} + u_{(i,j-1)}\}
\end{aligned}$$

Neumann boundary condition (24) on the airfoil surface is discretized as follows,

$$\frac{P_{I(i,2)} - P_{I(i,1)}}{\Delta\eta} = \frac{1}{Re}\left(\frac{h_2}{h_1}\frac{\partial\omega}{\partial\xi}\right)_{(i,3/2)} - (h_2 u\omega)_{(i,3/2)} - \left[h_2\frac{\partial v}{\partial t}\right]_{(i,3/2)} \tag{28}$$

To make LHM equal to zero, the above equation has been multiplied by $\frac{1}{\Delta\eta}[\frac{h_1}{h_2}]_{(i,3/2)}$ on both sides. Individual terms are discretized as indicated above. The last term of the right hand side is represented as,

$$\left[h_1 \frac{\partial v}{\partial t}\right]_{(i,3/2)} = -\frac{\partial}{\partial t}\left(\frac{\partial \psi_I}{\partial \xi}\right)_{(i,3/2)}$$

The right hand side quantities are obtained as central averages with individual quantities discretized using second order central difference scheme. Similarly, the Neumann boundary condition at the outer boundary is written as

$$\frac{P_{I(i,m-1)} - P_{I(i,m)}}{\Delta\eta} = \frac{1}{Re}\left(\frac{h_2}{h_1}\frac{\partial \omega}{\partial \xi}\right)_{(i,m-1/2)} - (h_2 u\omega)_{(i,m-1/2)} - \left[h_2 \frac{\partial v}{\partial t}\right]_{(i,m-1/2)} \tag{29}$$

This equation is multiplied by $\frac{1}{\Delta\eta}\left[\frac{h_1}{h_2}\right]_{(i,m-1/2)}$ to make LHM equal to zero. The discretization procedure is similar to that adopted for the Neumann boundary condition applied on the airfoil surface. Discretized equations are then solved using the conjugate-gradient algorithm of [**?**]. The above formulation of the PPE with the boundary condition of (24) is solved following the discretization as indicated above and it can also be solved by taking a smaller domain as compared to the domain used for solving SFEs and the VTE. This is due to the fact that the boundary condition used here are exact up to the accuracy by which the velocity and vorticity fields are numerically calculated.

2.4. Validation studies

To substantiate the methods and procedures followed in the present study, it is necessary that some unsteady flow cases be computed for which experimental results exist. Here we consider the unsteady accelerated flow past a NACA 0015 airfoil, for which results are available in [**?**] and [**?**]. In [**?**], the airfoil is set at 30^o angles of attack and the flow is computed for $Re = 35000$, with the oncoming free-stream speed varied as $U_o = U_\infty tanht/\tau$. The Reynolds number is calculated based on the chord of the airfoil and the final free-stream speed, as indicated at the top of Fig. 2. In the computation, the flow start-up is implemented through the Neumann boundary condition applied at the outflow for Eq. (17).

In Fig. 2, the computed streamline contours are compared with flow visualization picture of [**?**]. The final steady mean flow velocity is 64 cm/sec in dimensional units and τ is the characterstic acceleration time given by 50 ms- that is equal to 0.60 in the nondimensional unit used in the present formulation. The mean flow creates a non-uniform acceleration for a time upto 100 ms, beyond which the mean flow remains steady- but the unsteady effects persist much longer. The computed and experimental results shown in Fig. 2, corresponds to $t = 2.903$- a nondimensional time. It is noted that the computed flow field matches with all essential details of the experimental visualization data, in terms of size, shape and orientations of the primary, secondary and tertiary vortices.

Another case is considered here for validation studies, reported in [**?**], for NACA 0015 airfoil held at 30^o angle of attack, for which the flow is accelerated uniformly

from rest. The Reynolds number, which is based on the airfoil chord of 80 mm and the steady post-acceleration flow velocity of 100 mm/s, is 8000. Here the flow is accelerated from zero to the final flow velocity in 2 s duration by a constant amount for the case for which the acceleration rate is $50mm/s^2$. In the experiments, cross-correlation digital PIV results were measured. In Fig. 3, experimental results are compared with present computed ones. The displayed times in the figures correspond to the units used for the computations in nondimensional form. Once again the computed results match the details shown in the experimental results. The results of Figs. 2 and 3, shows the ability of the present method in computing unsteady flows.

The efficiency of the present method in computing the pressure field is assessed next by solving Eq. (23) in different truncated domains. In Fig. 4, comparison is made between solutions for the case of the flapping NACA 0014 airfoil (details in next section) for $Re = 20000$ using two different domains. While 300 points have been taken in the η- direction for computing the SFEs and the VTE, the PPE is solved with $m = 100$ and 150 points in the η- direction. Displayed contour values indicate the results as identical for the two domains. The computed lift and drag coefficients are shown below the contour plots for a short interval of time after $t = 80$. One can see that the integrated surface pressure and shear stress contributions to these coefficients yield exactly identical results. The number of points needed in the $\eta-$ direction to solve PPE depends upon the accuracy with which derivatives in the boundary conditions can be estimated at the outer boundary. Thus, $(\psi - \omega)$ formulation can be used with structured orthogonal grid while using fewer unknowns and the loads and moment can be calculated either on- or off-line using the velocity and vorticity solutions. The choice of 100 points in the η- direction is made based on some preliminary calculations made with different grids using different number of points in this direction. It is seen that increasing the number of points beyond 100 does not alter the results up to fourth decimal place and thus, these many points were considered to be adequate for solving the PPE. It appears that locating outer boundary below 100 points, numerically calculated derivatives in Eq. (24) are not accurate enough- this determines the dimension of the truncated domain for PPE.

It is important to highlight some aspects of various solvers used in this study, in association with their boundary conditions. Firstly, for unsteady flows, it is essential to tighten the convergence criterion for the solution of Eq. (17). Secondly, it was found that solution converges only in one out of two possible ways of implementing the accelerated start cases in the validation studies, when the Reynolds number is kept fixed to its final value and the velocity boundary conditions at the outflow is increased from zero to its final steady state value. The other possibility does not work for which the instantaneous velocity is taken as the scale and that imply fixing the velocity at the outer boundary, while the Reynolds number is changed progressively for VTE from zero to its final value. This manifests itself in non-convergence of solution for the SFE. For the VTE, the major source of numerical problem is the diffusion terms in Eq. (18) that is divided by the Reynolds number. For the range of Reynolds number chosen in the present study, this parameter is moderate, as compared to cases of aeronautical interests with Reynolds numbers varying in the range of 10^5 to 10^7. The reason for this problem is due to aliasing

error committed during the evaluation of the products of $\frac{h_2}{h_1}$ and $\frac{\partial \omega_r}{\partial \xi}$ for the first term and a similar product for the other diffusion term. Despite the fact that this is a linear term, the product appears due to grid transformation and the actual quantum of aliasing error depends sensitively on the used grids. In [**?**] a detailed account of this type of error is provided and not repeated here.

3. RESULTS AND DISCUSSION

Here Navier-Stokes equation is solved to explore the unsteady aerodynamics of flight at moderate Reynolds number when the airfoil under investigation executes complex oscillations in horizontal, vertical and pitch planes. Here, we report some results for the cases of (a) flapping motion by pure heaving oscillation- as in [**?**]; (b) hover motion created by pitching oscillation in combination to oscillation in the horizontal plane- the type of motion considered in [**?**] and [**?**] and (c) a combined flapping- hover mode motion of NACA 0014 airfoil at $Re = 20000$ to show the ability of the used numerical methods in computing highly unsteady aerodynamics. The aim of the present study is mainly to propose a consistent formulation of the problem and its high accuracy solution methods that can be used to study MAV and bird/insect flights. Presented results are typical of these flights and provide an initial set of results for complete viscous solution. The developed methodologies can be used to enhance understanding of the unsteady aerodynamics of such flows and are discussed below.

3.1. Flapping motion of an airfoil

In this mode, a case is considered that corresponds to that given in [**?**] for NACA 0014 airfoil at $Re = 20000$. Here, the airfoil executes pure heaving oscillation for zero angle of attack setting. The heaving oscillation amplitude is equal to $0.40c$ producing large perturbations to the oncoming flow. The reduced frequency of oscillation is given by $k = 0.4$. In Fig. 5, lift, drag and pitching moment (about mid-chord) coefficients are shown as a time series. The period of heaving oscillation is 16 and the presented results are for about five cycles. Corresponding pressure and vorticity contour plots are shown in Figs. 6 and 7 respectively. Pressure is calculated over a truncated domain whose rationale is already discussed with respect to Fig. 4. High values of lift is associated with downward stroke of the foil, while it is negative during the upstroke. In all the vorticity contour plots, negative contours are shown by dashed lines. The heaving motion of the foil causes the vortices to be ejected from the trailing edge and the jet-like eruptions explain the lift and thrust generation by the flapping of the airfoil. Present results show that a pure flapping motion is incapable of producing sustained thrust.

3.2. Second-hover mode of motion

In this mode, the airfoil executes combined oscillations in the horizontal and the pitch plane in a quiescent ambience- and is termed as the mode-2 hovering in [**?**] and [**?**]. Freymuth [**?**] also called this as the *degenerate figure of eight mode* or the *normal hovering mode*. For this case the mean angle of attack of the airfoil is held at ninety degrees with respect to the horizontal oscillation. In this case, the airfoil oscillates in still air and the reduced frequency of both the translating and pitching oscillation is taken the same. To define the Reynolds number for this

mode, a velocity scale is constructed with the help of the amplitude of horizontal oscillation. This is given by, $Re = k_x a_x c/\nu$, where the parameters have been defined in Eq. (8). The translational oscillation amplitude is taken for this case as equal to the chord of the airfoil. In [**?**], a 15% thick elliptic cylinder was considered to study various modes of hovering using only a (65×65) grid. Here, a NACA 0015 airfoil is considered instead using a much finer (257×300) orthogonal grid generated following the method of [**?**]. The airfoil pitches about the mid-chord with a phase difference of 90^o with respect to the translational oscillation. The pitch oscillation amplitude is 5^o about the mean angle of attack. The reduced frequencies of translational-pitching oscillation are taken as $k_x = k_\alpha = 1$. The computed case is for a Reynolds number of $Re = 27000$, as compared to 600 in the experiments of [**?**]. For the chosen reduced frequencies a single period of oscillation corresponds to unity.

In Fig. 8, time variation of lift, drag and pitching moment (about rotating center) coefficients are shown for this case. The displayed time interval in these figures covers ten cycles. Perturbations introduced by the large amplitude oscillations cause the lift and drag coefficients to have large excursions. It has been explained in [**?**] that in the absence of mean convection, with the combined translational and pitching oscillation, an inclined vortex-jet is established that produces large lift for the purpose of hover. For such motion, the streamline contours in the moving frame of reference is shown in Fig. 9 from $t = 7.50$ to 8.40. It is seen that a flow is established from below to the top of the airfoil, along with puff of vortices released from the leading and the trailing edge of the airfoil. Asymmetry of the foil causes the strength of these vortices to be dissimilar. This may suggest that for pure unsteady applications, one must use a geometry that retains a fore-aft symmetry as opposed to conventional aerofoils with sharp trailing edge that ensures steady flow. For this mode of motion, clearly thrust is generated over significant duration of the airfoil motion in each cycle. Pressure and vorticity contours plots for this case are shown in Figs. 10 and 11. Large values of the load coefficients are needed for this mode of motion- as the dynamic pressure levels are very low, for the choice of the velocity scale in the absence of mean motion.

3.3. Combined flapping-hover mode of motion

From the results of previous sub-sections, it is seen that pure flapping and hover motion can create significant amount of lift- but pure flapping cannot create sustained thrust. In [**?**], it is conjectured that flapping mode of motion experiences lesser drag than the non-articulated stationary airfoil set at the mean angle of attack. However, our results do not show this for significant period of time. Pure hover mode considered in the previous subsection can create large amount of unsteady lift. However, to explain sustained non-accelerated level flights of insect and birds, more complex motion of the wing needs to be considered. For example, high values of lift is created during the clap-fling mechanism of Weis-Fogh exhibit simultaneous flapping and rotation of the insect wing. This specifically affects the phase (or time) lag between the attainment of instantaneous lift and the shed vorticity in the wake. While this requires systematic optimal search of such motion, we report a computed case where an airfoil executes simultaneous oscillation in heaving, pitching and horizontal motion. Once again, NACA 0014 airfoil is consid-

ered for flow at $Re = 20000$ with the mean angle of attack set at zero incidence. In Eqs. (8)-(10) the following parameters have been considered: $a_x = a_y = 0.5c$; $k_x = k_y = k_\alpha = 2\pi$; $\alpha_a = 5^o$ and $\phi_1 = \phi_2 = 0$. It is to be emphasized that these parameters are chosen to compute a case that is tough computationally due to very high unsteadiness of the flow field.

Fig. 12 shows the trajectory of the airfoil motion and the resultant loads and pitching moment experienced by the foil. The motion of the airfoil is shown parametrically on the top frame. Displayed trajectory of the foil is due to a combined flapping and hovering motion with large amplitudes and frequencies. Such large amplitude motions are not usually seen in natural flyers. Below the trajectory- lift, drag and pitching moment (about the rotation center) coefficients are shown as a function of time. For the choice of reduced frequency of oscillations the time period is close to unity and the shown results are for about ten cycles. It is seen that the loads follow two predominant time scales and to understand the sequence of events, one full cycle has been identified in Fig. 12 between $t = 7.25$ to 8.25. The point-A in the trajectory corresponds to when the foil is retreating and coming down to its extreme position at B. Around this extreme position- the lift fluctuates- however, the level remains around the secondary maximum at B. During this phase, the drag experienced by the foil comes down and eventually becomes a suction force, while the pitching moment about the rotation center progressively becomes nose-up. During the early phase of upswing motion of the foil the lift decreases and the drag reduces at a rapid rate to its global minimum. The pitching moment increases during this stage. In the next phase of motion C_l increases to its global maximum while C_d and C_m decreases to their global minimum. During the upstroke, the lift value remains at around its global maximum.

In Fig. 13, streamline contours for ψ_r are plotted in the moving frame of reference to understand the physical events responsible for the extrema of load values indicated in Fig. 12. During the early phase, the front stagnation point is at mid-chord on the lower surface of the foil and a dynamic stall vortex (DSV) is seen to grow on the top surface. This attached vortex continues to grow to its maximum position at $t = 7.516$. Large amplitude flapping and hover motion are responsible for the creation of massive strength DSV. For pure pitch oscillation of dynamic stall event or during accelerated start of flow, DSVs are also seen that are weaker in strength. At $t = 7.516$, one notes the formation of a saddle point upstream of the airfoil- marked in the frame as A. Appearance of the singular point is followed by a rapid clockwise rotation of the flow field between $t = 7.516$ and 7.616, that is also observed in [**?**] during the creation of large lift when a jet of fluid is ejected downward. This is also noted during the same time as the motion of a vortex-doublet (identified as B and C in the frames). Also, at $t = 7.616$, one notices the formation of a bubble on the lower surface near the trailing edge.

The vorticity contours for this case are shown in Fig. 14- during the same time interval of Fig. 13. Very strong coherent vortices are created due to the combined flapping and hover mode of motion. These are seen whenever the DSV is formed near the leading edge on top surface (during $t = 7.316$ to 7.616) and when attached bubbles are formed on lower surface (during $t = 7.716$ and 7.816) near the trailing edge.

Pressure around the foil is calculated by solving the PPE in the truncated domain- as before, for this case and the contour plots are shown in Fig. 15, with the negative contours shown by dotted lines.

4. SUMMARY

An improved formulation and numerical method is reported here for calculating highly unsteady aerodynamics for hovering and flapping airfoil in two- dimensional flows. A correct formulation is solved by using high accuracy compact scheme for the VTE. A new method is used here to solve the governing pressure Poisson equation using a non-staggered grid in a truncated part of the computational domain that is used to solve the SFE and VTE. The developed methods are further speeded up significantly by using a high order filter after each time step of integration. The numerical methodology is validated with experimental results for two cases of flow past NACA 0015 airfoil at large angle of attack, for which the oncoming flow has been established with different types acceleration for Reynolds numbers of 8000 and 35000.

This method is then used to compute flow past NACA 0014 and 0015 airfoils executing flapping and hovering mode of motion, at typical Reynolds numbers to study unsteady aerodynamics relevant to MAV and insect/ bird flight. While the flapping and hovering mode of motion is studied that indicates the creation of high unsteady lift and thrust, a combined flapping-hover mode motion has also been computed here for very large amplitude motion of the airfoil to show the efficacy of the developed method for solving the viscous flow.

ACKNOWLEDGMENT

The authors would like to acknowledge Srikanth B. Talla, in helping develop the method for solving the PPE. We also acknowledge Profs. Soria and Lim for providing us with good quality pictures of their experiments that have been used to validate the numerical methods. Finally, we also acknowledge the referees for many useful suggestions for improving the text.

REFERENCES

1. K.V. Rozhdestvensky and V.A. Ryzhov, Aerohydrodynamics of flapping-wing propulsors, Prog. Aerospace Sci. **39**, 585-633 (2003)
2. S. Ho, H. Nassef, N. Pornsinsirirak, Y.-C. Tai and C.M. Ho, Unsteady aerodynamics and flow control for flapping wing flyers, Prog. Aerospace Sci. **39**, 635-681 (2003)
3. Y. Lian, W. Shyy, D. Viieru and B. Zhang, Membrane wing aerodynamics for micro air vehicles, Prog. Aerospace Sci. **39**, 425-465 (2003)
4. S.P. Sane, The aerodynamics of insect flight, J. Exp. Biology, **206**, 4191-4208 (2003)
5. U.M. Norberg, *Vertebrate flight: Mechanics, physiology, morphology, ecology and evolution*, Springer, New York (1990)
6. C.J. Pennycuick, Actual and 'optimum' flight speeds: field data reassessed, J. Exp. Biology, **200** 2355-2361 (1997)
7. B.W. Tobalske and K.P. Dial, Flight kinematics of black-billed magpies and pigeons over a wide range of speed, J. Exp. Biology, **199**, 263-280 (1996)
8. W. Nachtigall, *Insects in flight* Mc-Graw Hill, New York (1974)
9. P. Freymuth, Thrust generation by an airfoil in hover modes, Experiments in Fluids, **9**, 17-24 (1990)
10. J.D. DeLaurier, An aerodynamic model for flapping wing flight, Aeronautical J., **97** 125-130 (1993)
11. G.R. Spedding, The aerodynamics of flight. Adv. Comp. Env. Physiology, **11**, 51-111 (1992)
12. M. Sun and J. Tang, Lift and power requirements of hovering flight in *Drosophila virilis*, J. Exp. Biology, **205** 2413-2427 (2002)
13. S.E. Rogers and D. Kwak, Upwind differencing scheme for the time-accurate incompressible Navier-Stokes equation, AIAA J. **28** 253-262 (1990)
14. T.K. Sengupta and A. Dipankar, A comparative study of time advancement methods for solving Navier- Stokes equations, J. Sci. Comp. **21(2)** 225-250 (2004)
15. Z.J. Wang, Vortex shedding and frequency selection in flapping flight, J. Fluid Mech. **410** 323-341 (2000)
16. K. Gustafson and R. Leben, Computation of dragonfly aerodynamics, Computer Physics Communications, **65** 121-132 (1991)
17. K. Gustafson, R. Leben and J. McArthur, Lift and thrust generation by an airfoil in hover modes, Comput. Fluid Dyn. J. **1(1)**, 47-57 (1992)
18. W. E and J.-G. Liu, Essentially compact schemes for unsteady viscous incompressible flows, J. Comput. Phys. **126** 122- (1996)
19. P.J. Roache, *Computational Fluid Dynamics*, Hermosa Publishers, New Mexcio, USA (1976)
20. T.K. Sengupta, A. Kasliwal, S. De and M. Nair, Temporal flow instability for Magnus-Robins effect at high rotation rates, J. Fluids Struct. **17**, 941-953 (2003)
21. M.T. Nair and T.K. Sengupta, Orthogonal grid generation for Navier- Stokes computations, Int. J. Num. Meth. in Fluids **28** 215-224 (1998)
22. S. Abdallah, Numerical solutions for the pressure Poisson equation with Neumann boundary conditions using a non-staggered grid-I, J. Comput. Phys. **70**, 182-192 (1987)
23. P.M. Grescho and R.L. Sani, On pressure boundary conditions for the incompressible Navier-Stokes equation, Int. J. Num. Methods Fluids, **7**, 1111-1145 (1987)
24. J.R. Clayssen, R.B. Platte and E. Bravo, Simulation in primitive variables of incompressible flow with pressure Neumann condition, Int. J. Num. Methods Fluids, **30**, 1009-1026 (1999)
25. K.D. Jones, B.M. Castro, O. Mahmoud, S.J. Pollard, M.F. Platzer, M.F. Neef, K. Gonet and D. Hummel, A collaborative numerical and experimental investigation of flapping-wing propulsion. AIAA paper no. **AIAA-2002-0706** (2002)
26. W.J. McCroskey, Unsteady airfoils, Ann. Rev. Fluid Mech., **24**, 285-311 (1982)
27. L.W. Carr, Progress in analysis and prediction of dynamic stall, J. Aircraft, **25(1)**, 6-17 (1988)
28. W.G. Bousman, Airfoil dynamic stall and rotorcraft maneuverability, NASA TM-2000-209601 (2000)

29. E. Berton, C. Maresca and D. Favier, A new experimental method for determining local airloads on rotor blades in forward flight, Expt. in Fluids, **37(3)**, 455-457 (2004)

30. G.E. Schneider and M. Zedan, A modified strongly implicit procedure for the numerical solution of field problems, J. Numer. Heat Transfer **4**, 1-19 (1981)

31. T.K. Sengupta, *Fundamentals of CFD* Universities Press, Hyderabad, India (2004)

32. T.K. Sengupta, A. Guntaka and S. Dey, Navier-Stokes solution by new compact scheme for incompressible flows, J. Sci. Comput. **21(3)**, 269-282 (2004)

33. T. K. Sengupta, G. Ganeriwal, and S. De, Analysis of central and upwind compact schemes, J. Comput. Phys. **192**, 677-694 (2003)

34. M.R. Visval and D.V. Gaitonde, On the use of higher order finite- difference schemes on curvilinear and deforming meshes, J. Comput. Phys. **181**, 155-185 (2002)

35. H.A. Van Der Vorst, Bi-CGSTAB: A fast and smoothly converging variant of Bi-CG for the solution of nonsymmetric linear systems, SIAM J. Sci. Stat. Comput. **13(2)** 631-644 (1992)

36. K. Morikawa and H. Grönig, Formation and structure of vortex systems around a translating and oscillating airfoil, Z. Flugwiss. Weltraumforsch. **19**, 391–396 (1995)

37. J. Soria, T.H. New, T.T. Lim and K. Parker, Multigrid CCDPIV measurements of accelerated flow past an airfoil at an angle of attack of 30^o, Experimental Thermal and Fluid Science. **27**, 667-676 (2003)

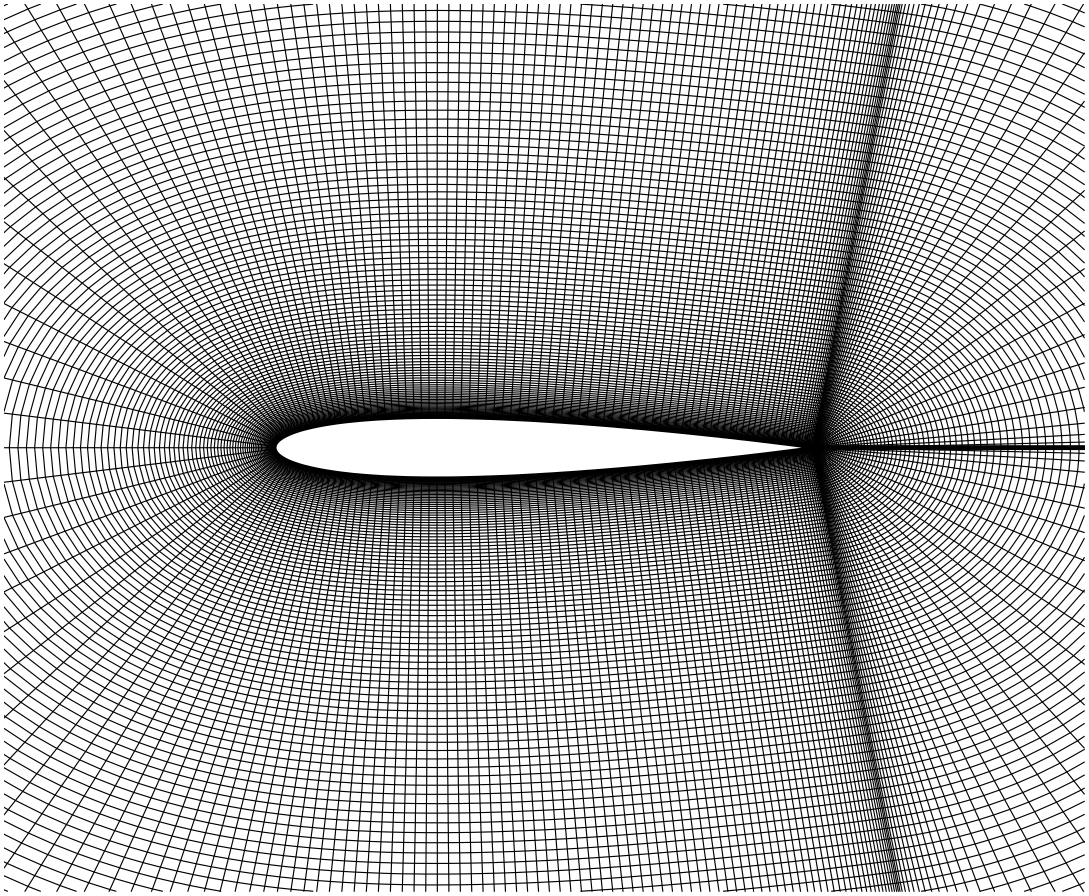

Fig. 1. Orthogonal (257x300)-grid generated by the hyperbolic grid generation method of [20]. Only the grids near the aerofoil surface are shown.

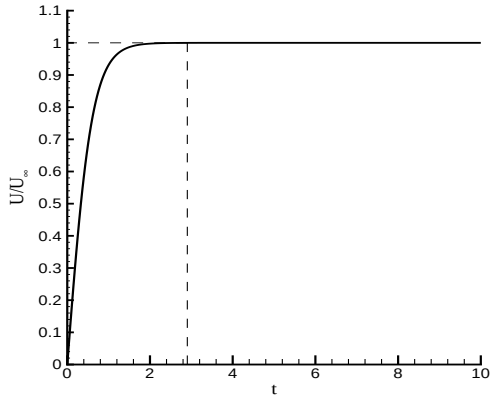

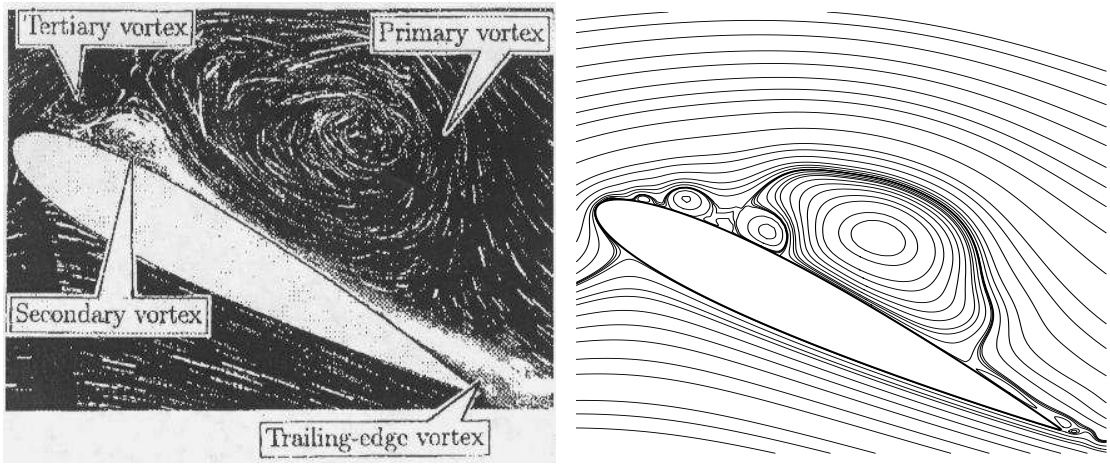

Fig. 2. Flow visualisation picture (bottom-left) compared with the computed streamline contour plot (bottom-right) at $t = 2.903$ for $Re = 35000$ and $\alpha = 30^o$ when the oncoming velocity changes with time as shown on top.

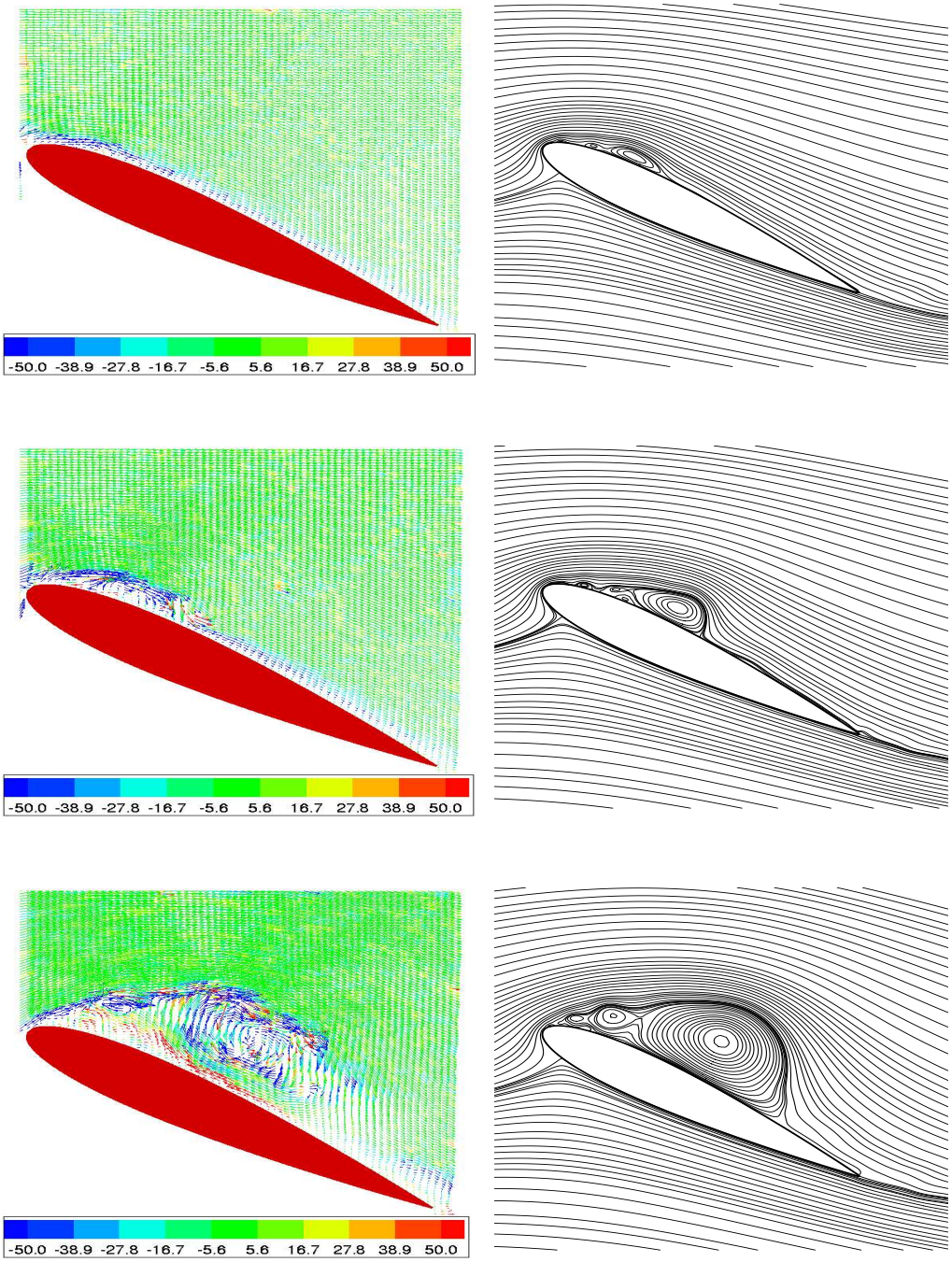

Fig. 3. Comparison of flow visualisation pictures obtained from PIV measurements with the computed streamlines at non-dimensional $t = 1, 2$ and 3 for $Re = 8000$ and $\alpha = 30^o$. Here the free stream velocity changed with a uniform acceleration of $50mm/s^2$ upto $t = 2.5$.

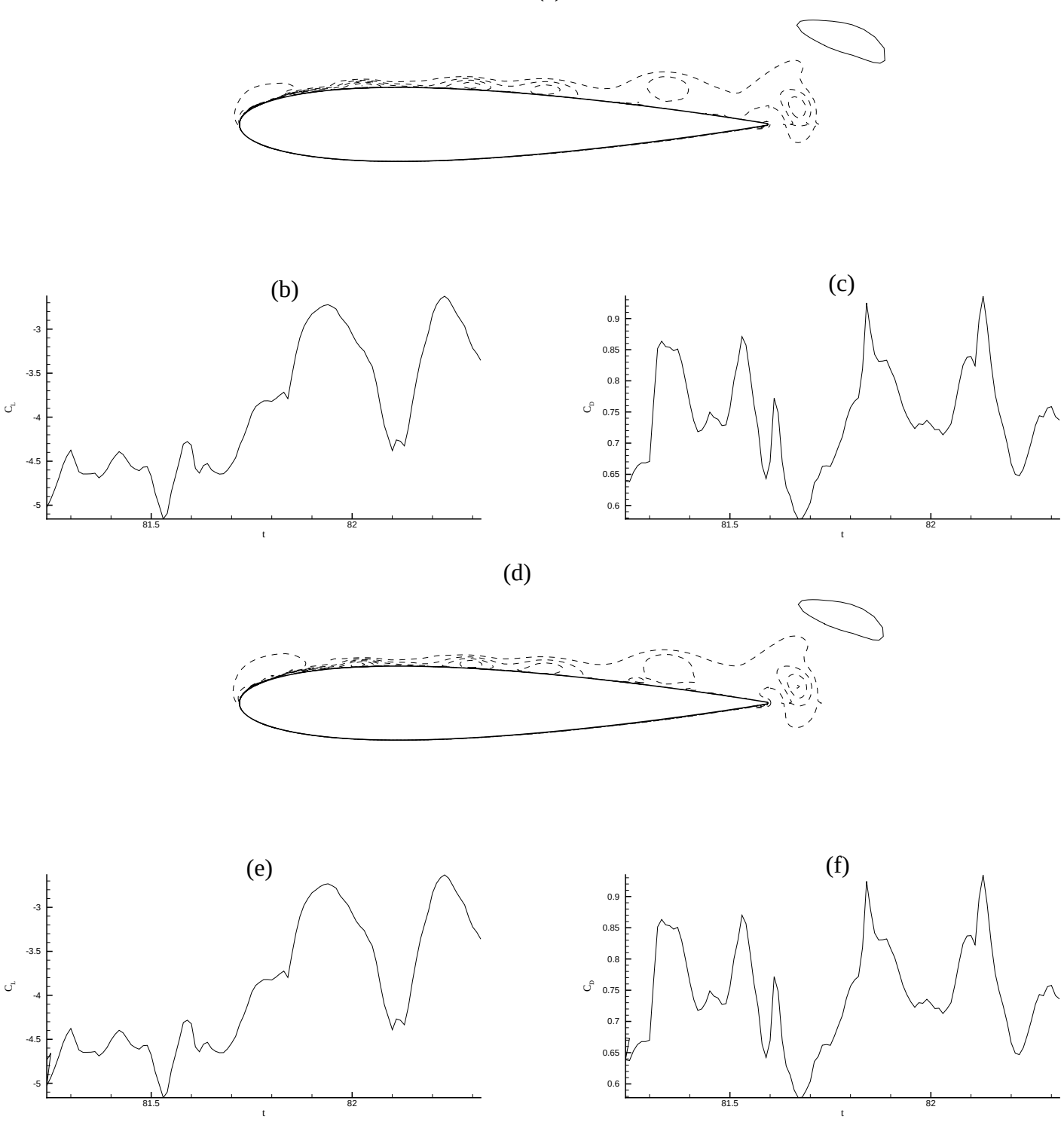

Fig. 4. Solution of PPE using two different values of m. (a) to (c) are for m=100 and (d) to (f) are for m=150. In (a) and (d) the pressure contours are shown; (b) and (e) show the lift variation with time and (c) and (f) show the variation of drag coefficient with time.

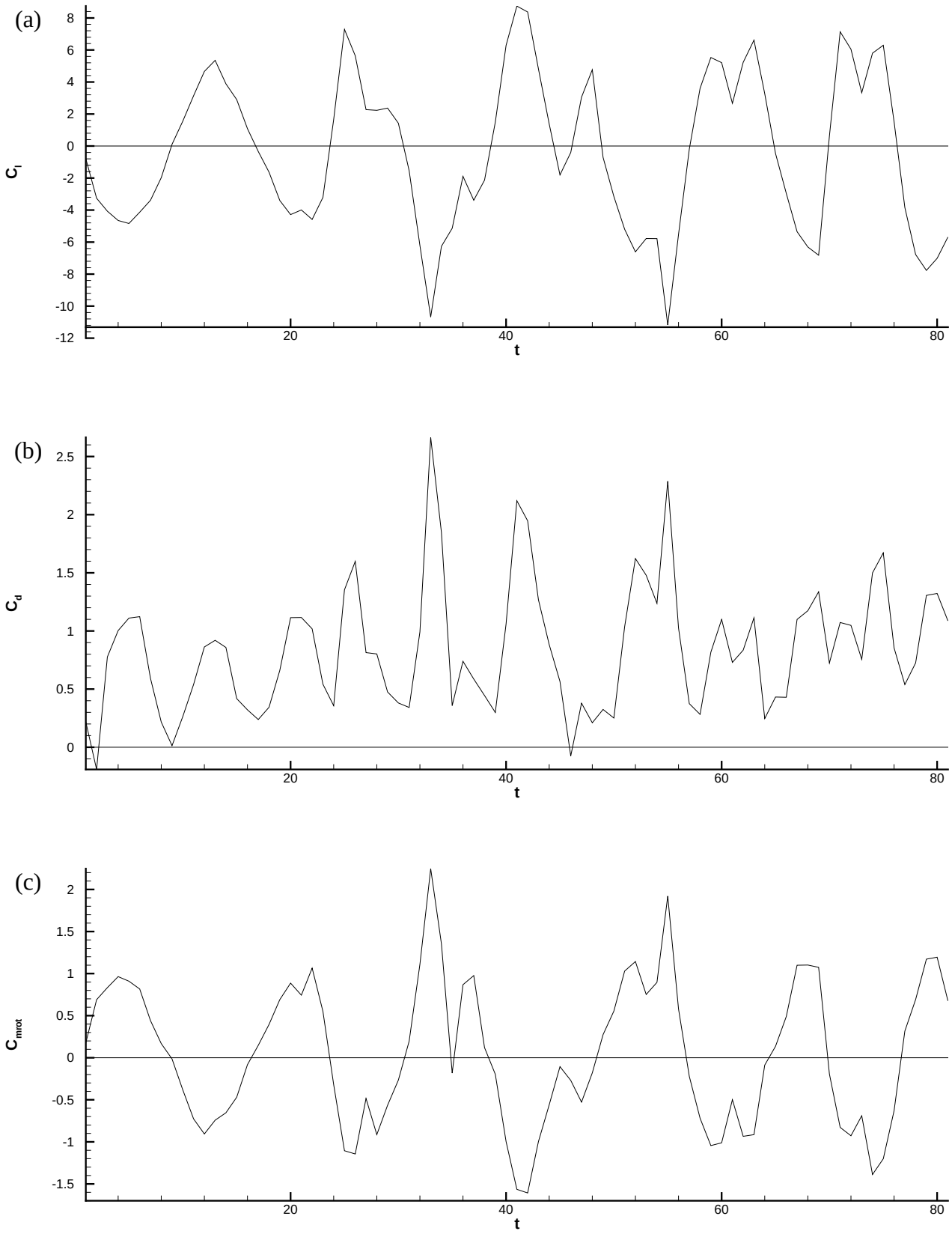

Fig.5. Loads vs time for flapping airfoil. Shown are (a) C_l vs time; (b) C_d vs time and (c) C_{mrot} vs time

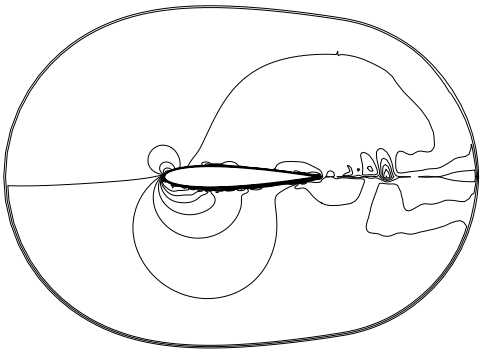

t=63

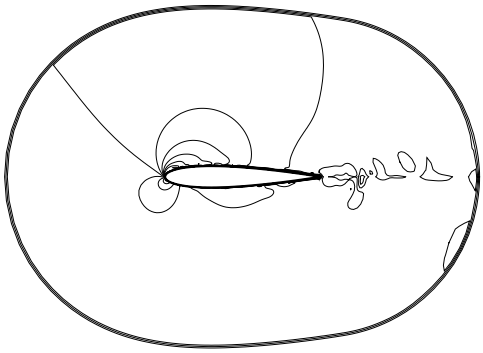

t=66

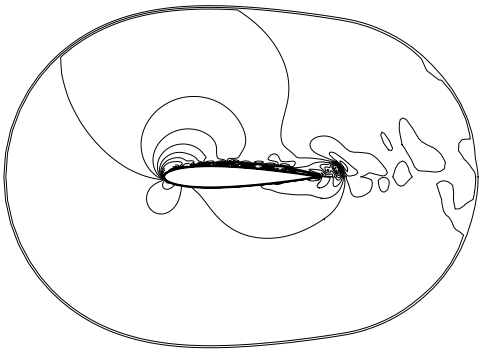

t=69

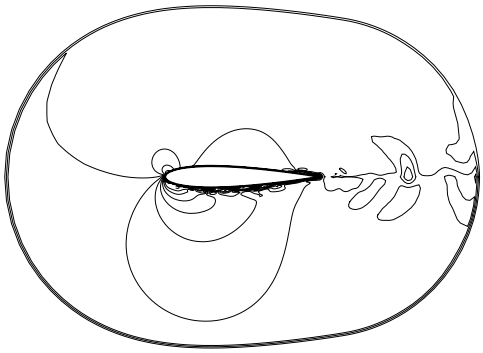

t=72

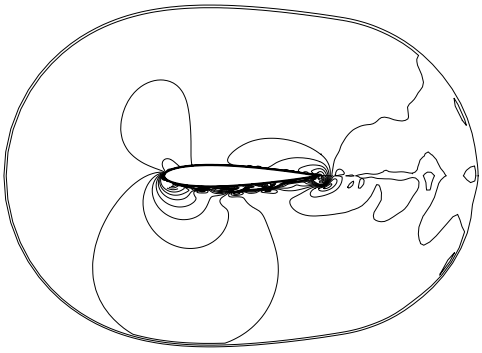

t=75

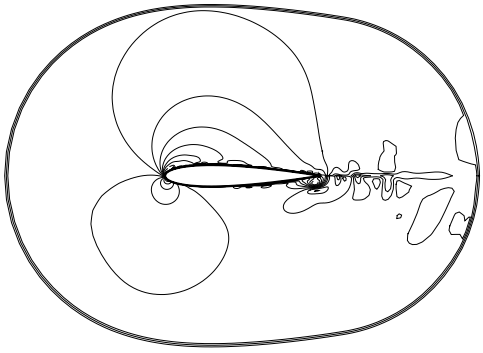

t=78

Fig.6. Pressure contours at indicated times for flapping airfoil. Dashed lines are negative contours.

t=66

t=69

t=72

t=75

t=78

t=81

Fig.7. Vorticity contours at indicated times for flapping airfoil. Dashed lines are negative contours.

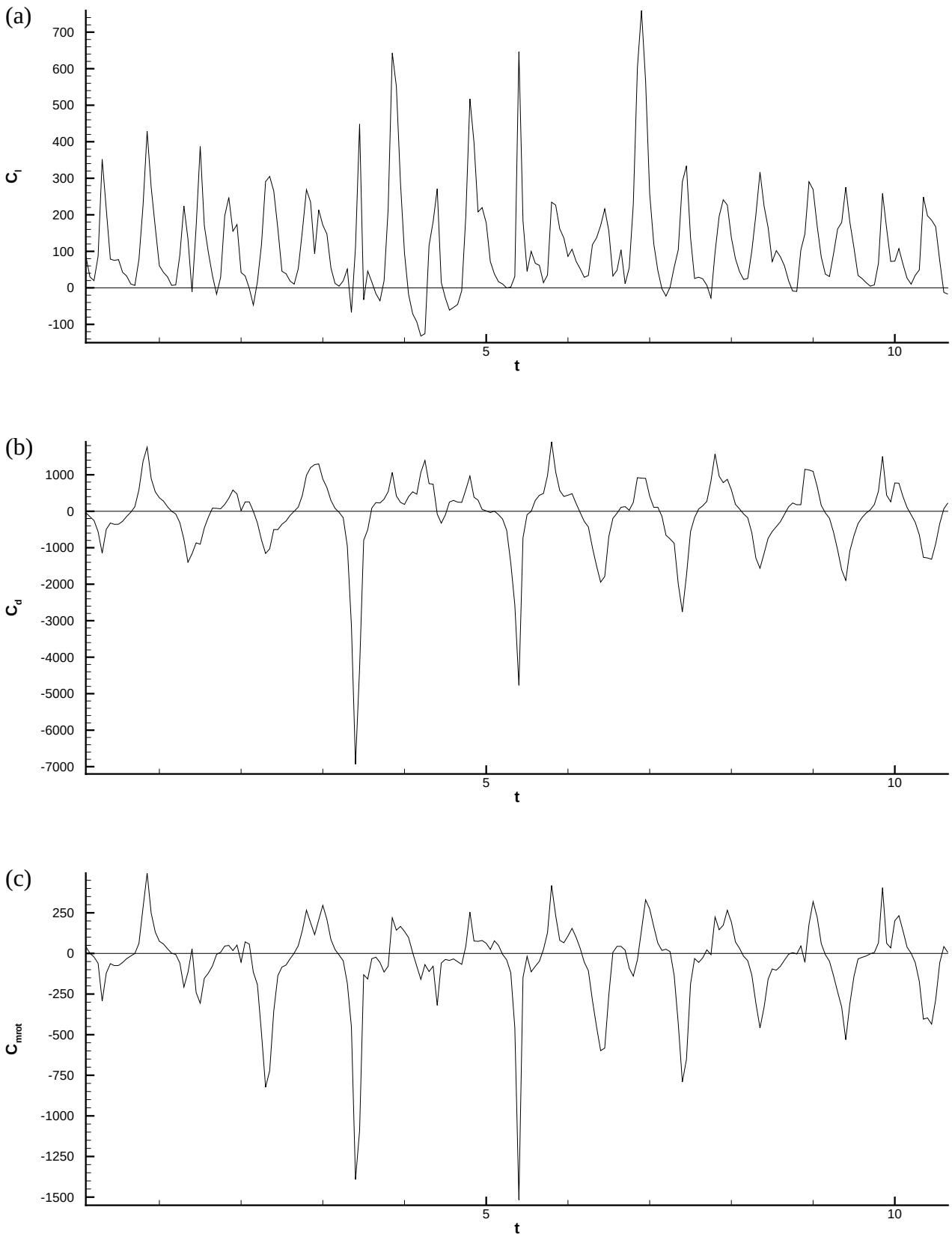

Fig.8. Loads vs time for hover mode motion. Shown are (a) C_l vs time; (b) C_d vs time and (c) C_{mrot} vs time

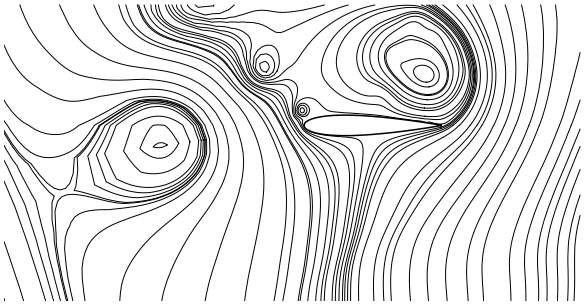

t=7.50

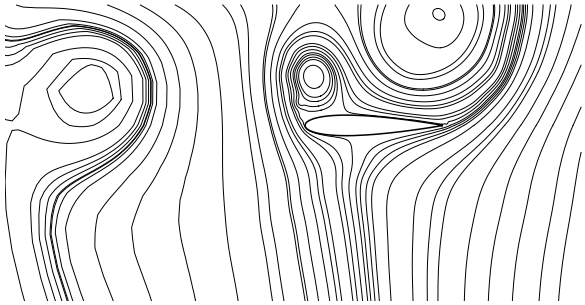

t=7.60

t=7.70

t=7.80

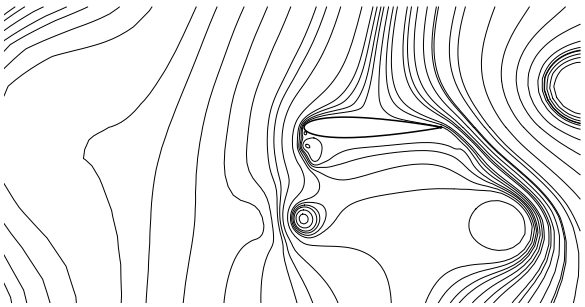

t=7.90

t=8.00

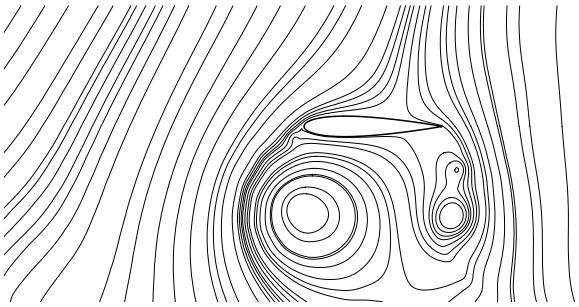

t=8.10

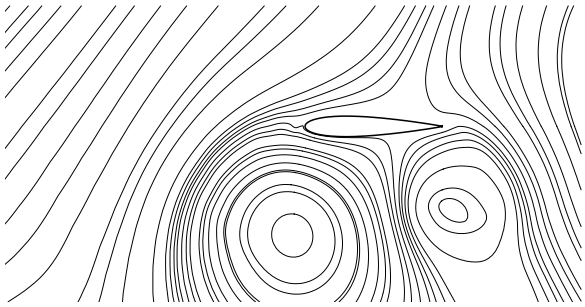

t=8.20

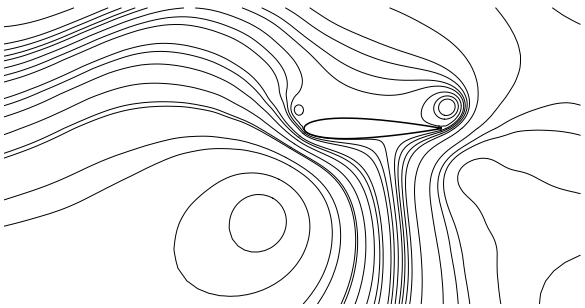

t=8.30

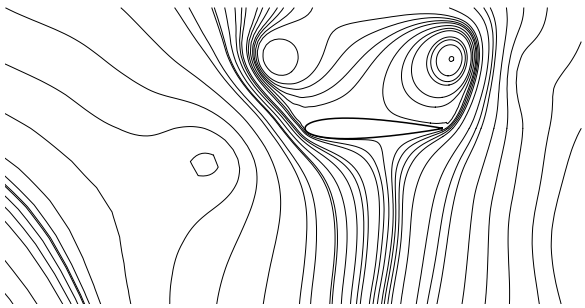

t=8.40

Fig.9. Streamlines in moving body-fixed frame at indicated times for hover mode motion.

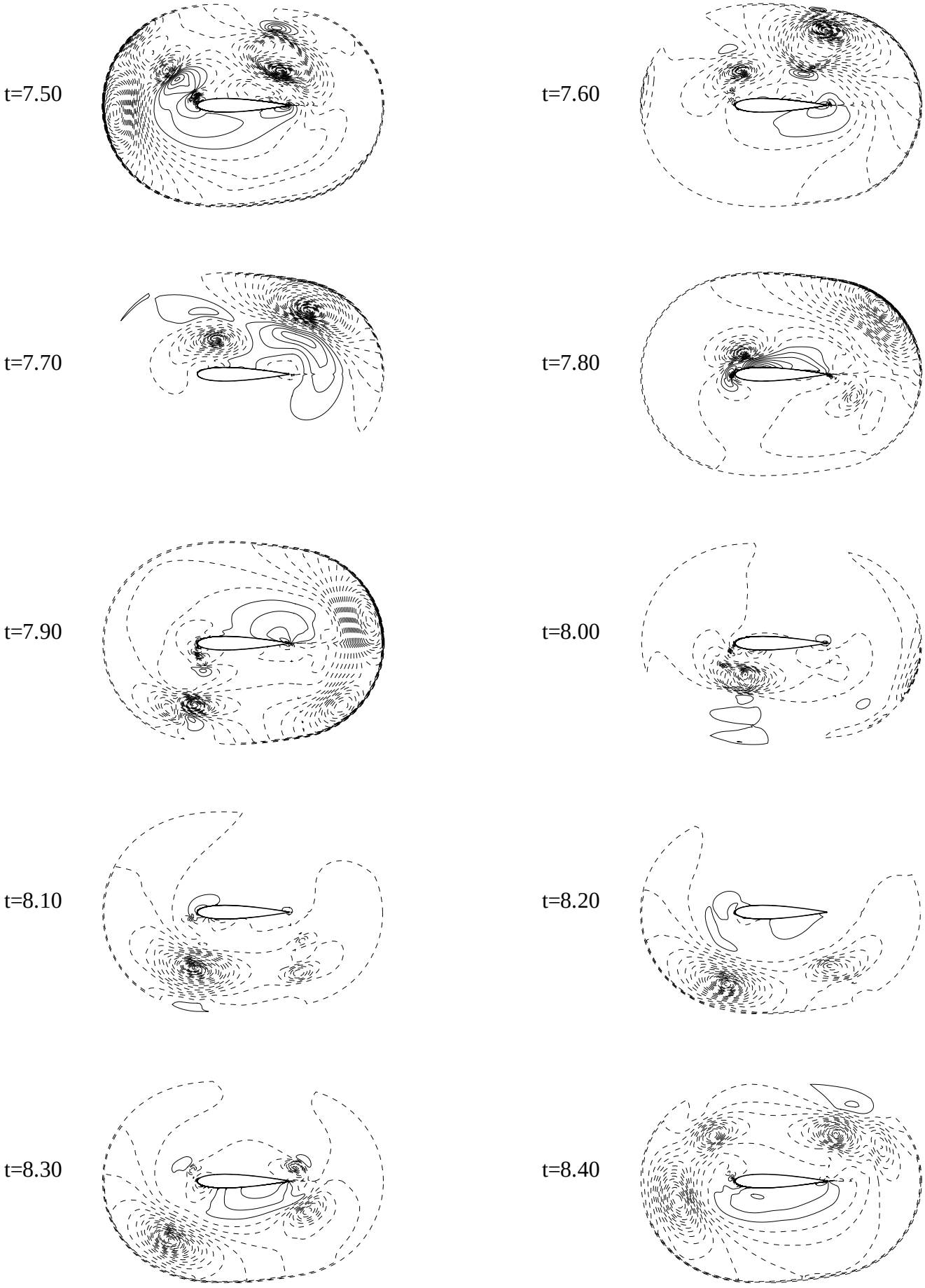

Fig.10. Pressure contours in moving body-fixed frame at indicated times for hover mode motion. Dashed lines are for negative contours.

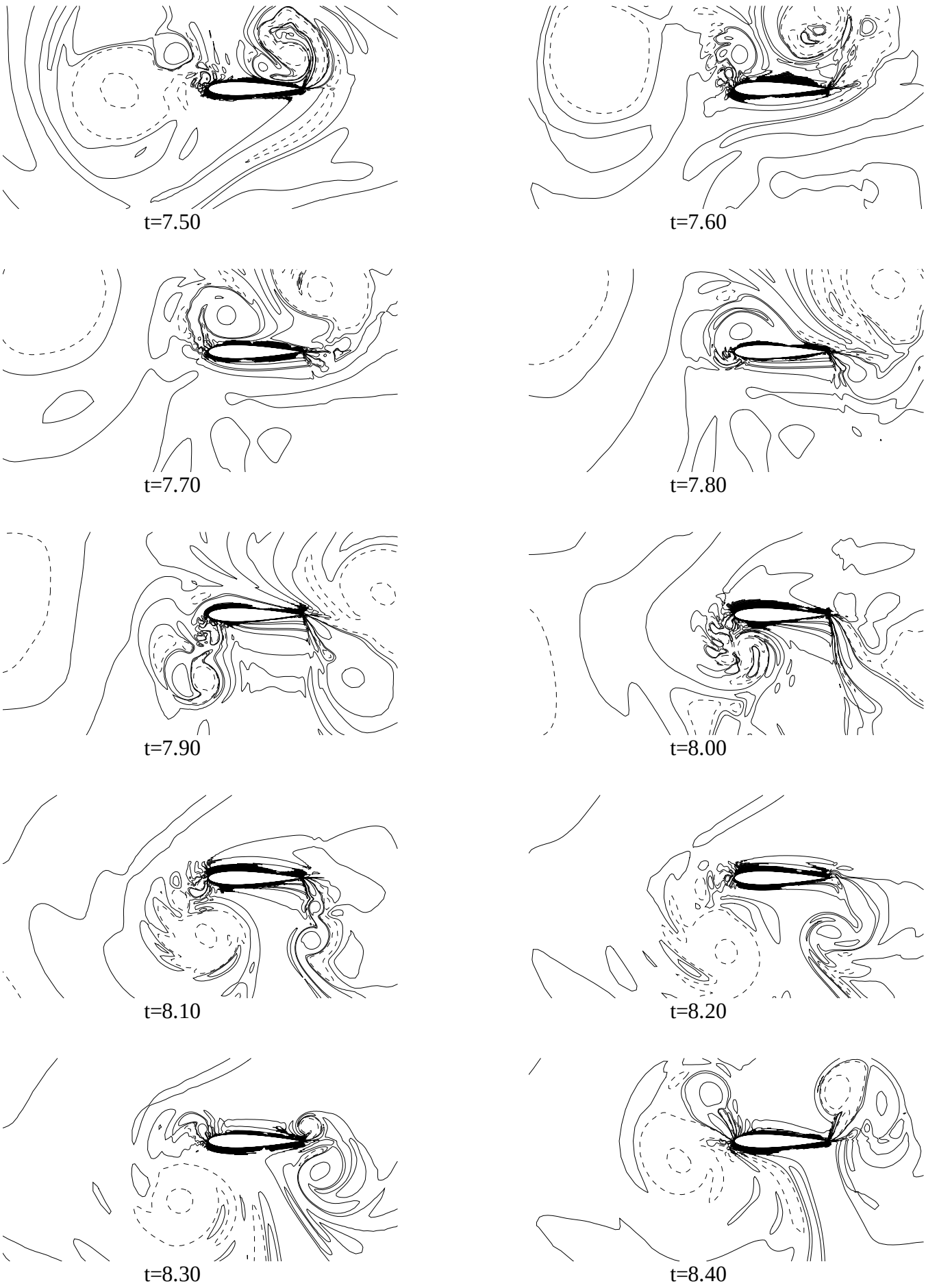

Fig.11. Vorticity contours in moving body-fixed frame at indicated times for hover mode motion. Dashed lines are for negative contours.

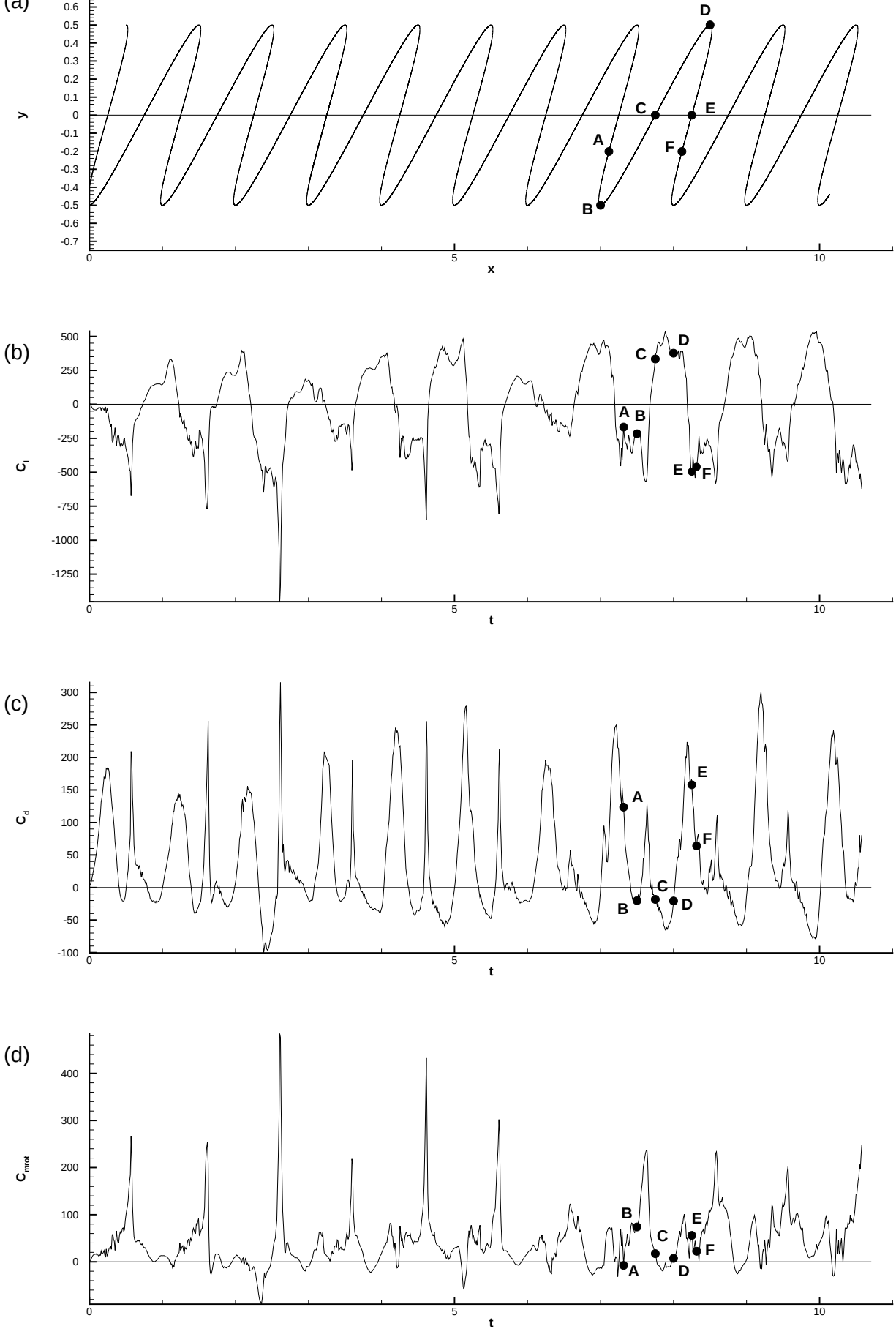

Fig.12. Trajectory and loads vs time for combined flapping and hover mode motion. Shown are (a) the trajectory of the airfoil motion; (b) C_l vs time; (c) C_d vs time and (d) C_{mrot} vs time

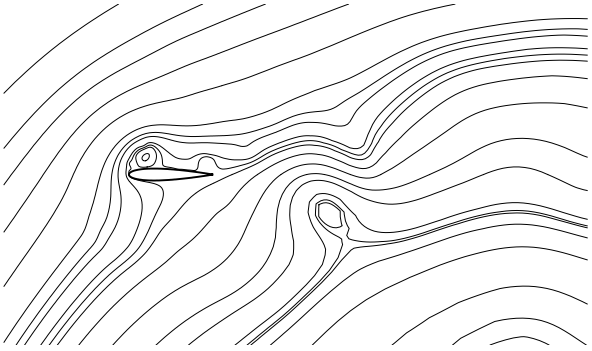

t = 7.316

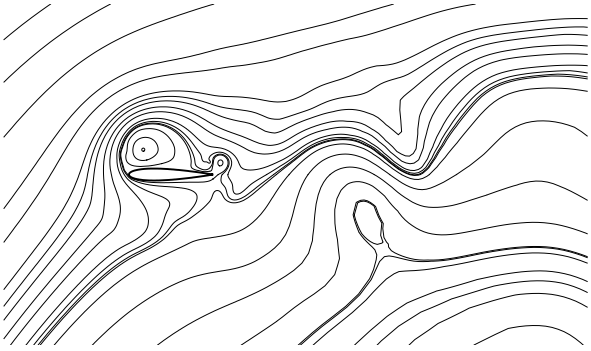

t = 7.416

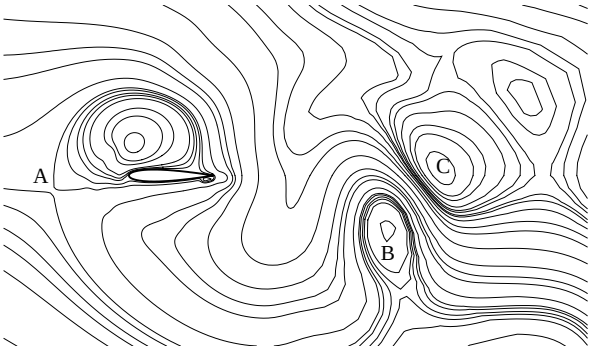

t = 7.516

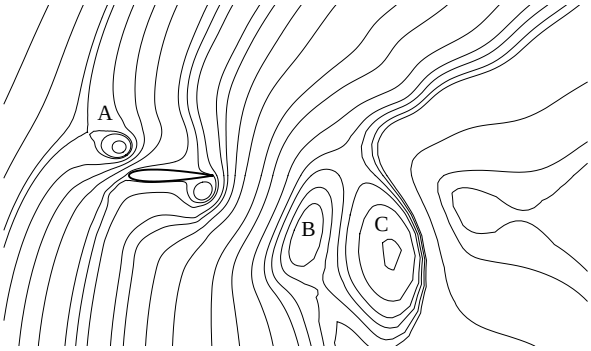

t = 7.616

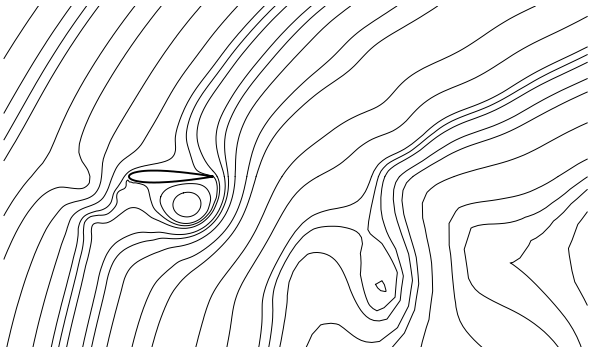

t = 7.716

t = 7.866

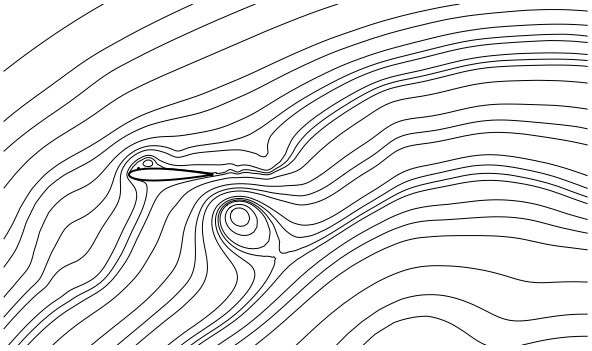

t = 8.166

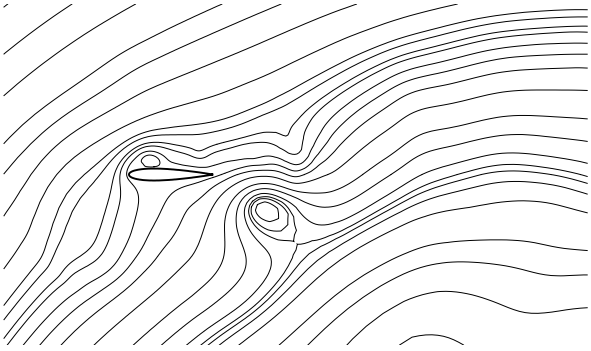

t = 8.216

Fig.13. Streamlines in the moving body-fixed frame at indicated times for combined flapping and hover mode motion.

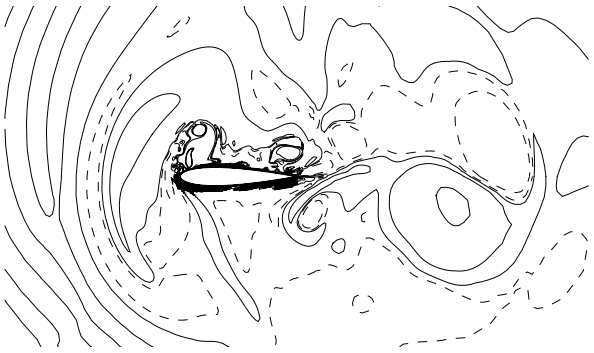

t = 7.316

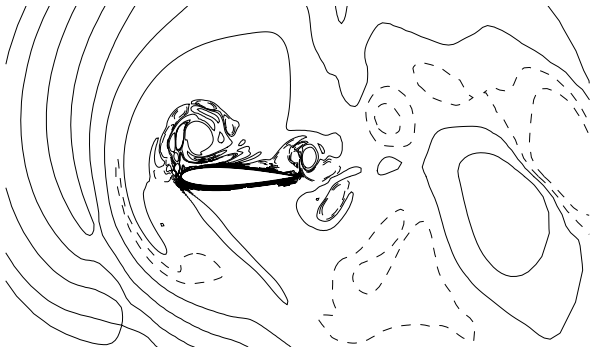

t = 7.416

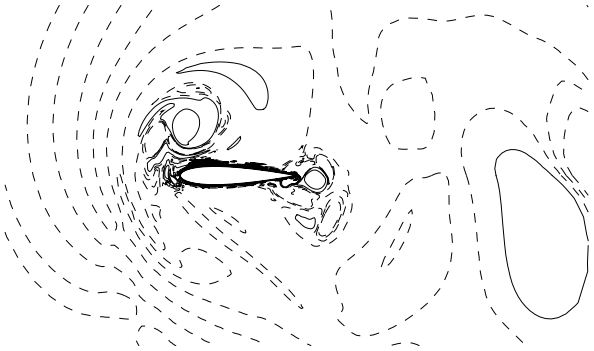

t = 7.516

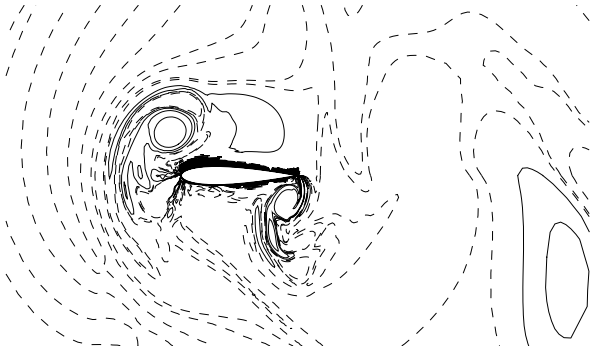

t = 7.616

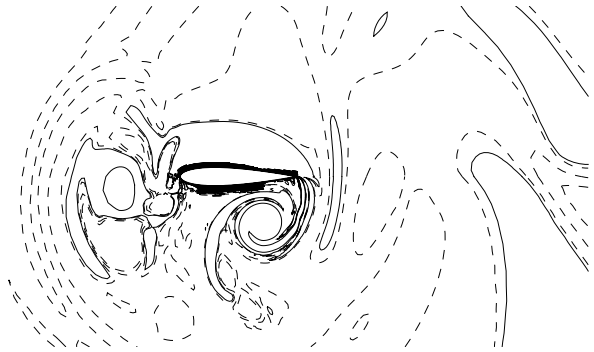

t = 7.716

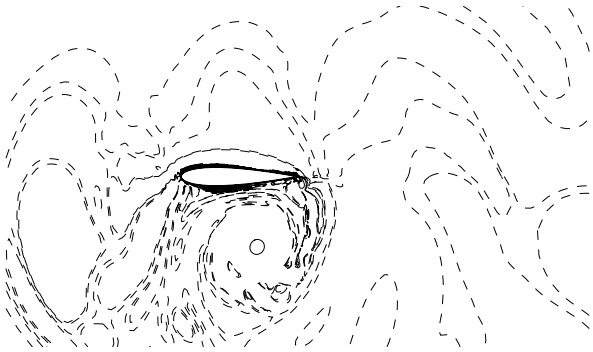

t = 7.866

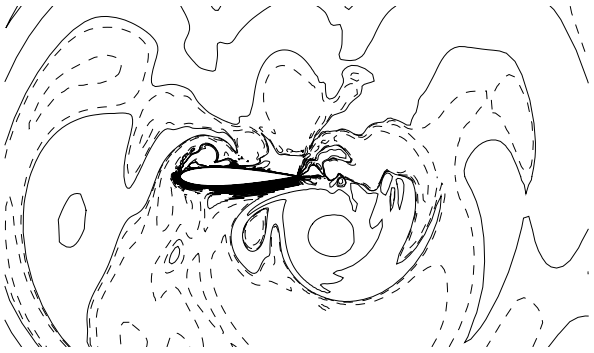

t = 8.166

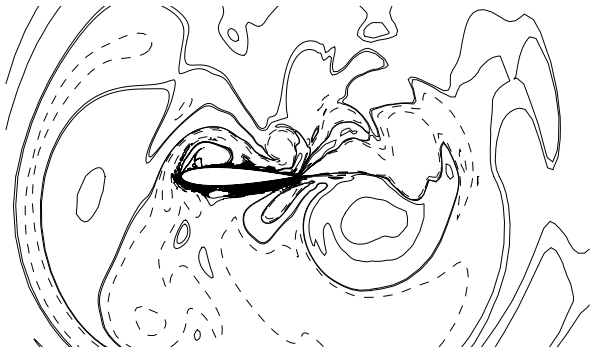

t = 8.216

Fig.14. Vorticity contours in the moving body-fixed frame at indicated times for combined flapping and hover mode motion. Dashed lines are for negative contours.

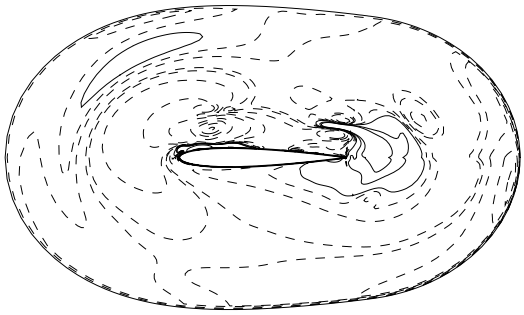

t = 7.316

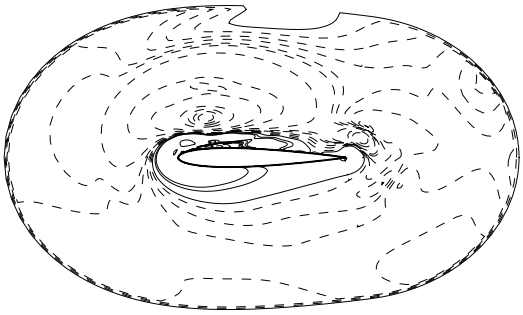

t = 7.416

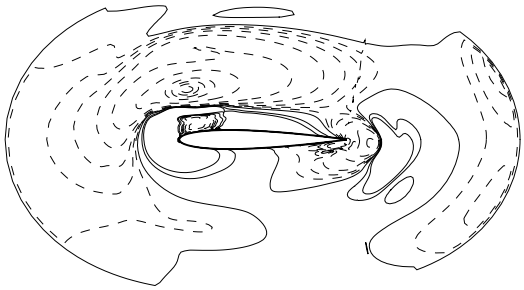

t = 7.516

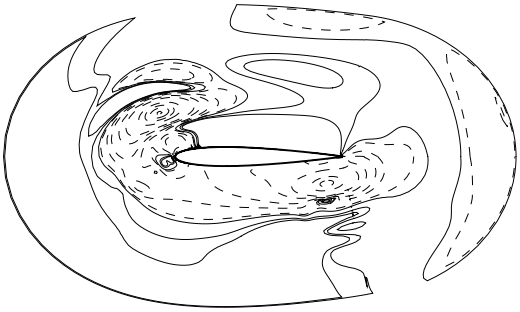

t = 7.616

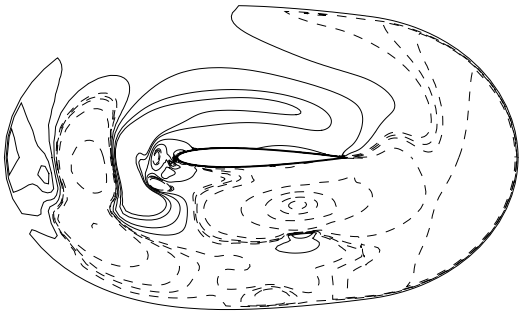

t = 7.716

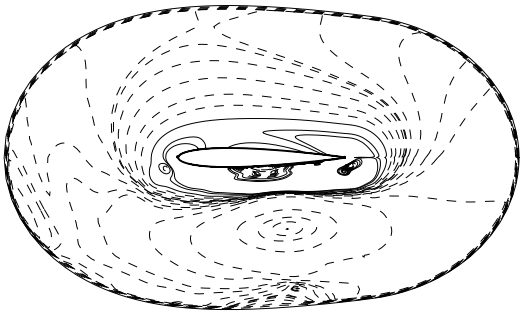

t = 7.866

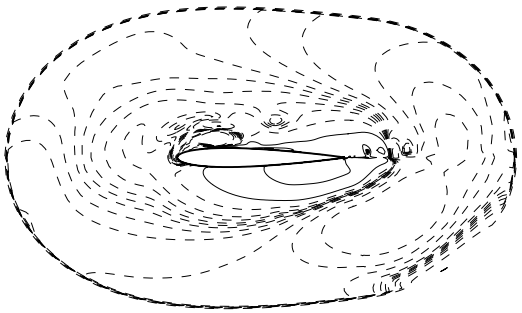

t = 8.166

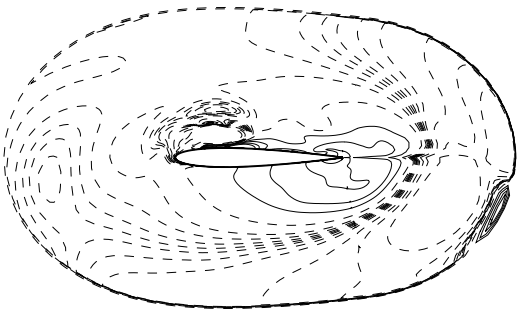

t = 8.216

Fig. 15. Pressure contours in the moving body-fixed frame at indicated times for combined flapping and hover mode motion. Dashed lines are for negative contours.